Magnetosheath high-speed jets: internal structure and interaction with ambient plasma

F. Plaschke[1], T. Karlsson[2], H. Hietala[3], M. Archer[4,5], Z. Vörös[6,1], R. Nakamura[1], W. Magnes[1], W. Baumjohann[1], R. B. Torbert[7], C. T. Russell[3], B. L. Giles[8]

[1]Space Research Institute, Austrian Academy of Sciences, Graz, Austria
[2]Space and Plasma Physics, School of Electrical Engineering, KTH Royal Institute of Technology, Stockholm, Sweden
[3]Department of Earth, Planetary, and Space Sciences, University of California Los Angeles, CA, USA
[4]School of Physics and Astronomy, Queen Mary University of London, London, UK
[5]The Blackett Laboratory, Imperial College London, UK
[6]Institute of Physics, University of Graz, Graz, Austria
[7]Institute for the Study of Earth, Oceans, and Space, University of New Hampshire, Durham, NH, USA
[8]NASA Goddard Space Flight Center, Greenbelt, MD, USA

Key Points:

- Rich internal jet structure resolved for the first time revealing large amplitude variations
- There are indications of jets stirring ambient magnetosheath plasma causing anomalous sunward flows
- Jets modify magnetosheath magnetic field aligning it with their propagation direction

Corresponding author: Ferdinand Plaschke, `ferdinand.plaschke@oeaw.ac.at`

Abstract

For the first time, we have studied the rich internal structure of a magnetosheath high speed jet. Measurements by the Magnetospheric Multiscale (MMS) spacecraft reveal large-amplitude density, temperature, and magnetic field variations inside the jet. The propagation velocity and normal direction of planar magnetic field structures (i.e., current sheets and waves) are investigated via four-spacecraft timing. We find structures to mainly convect with the jet plasma. There are indications of the presence of a tangential discontinuity. At other times, there are small cross-structure flows. Where this is the case, current sheets and waves overtake the plasma in the jet's core region; ahead and behind that core region, along the jet's path, current sheets are overtaken by the plasma, i.e., they move in opposite direction to the jet in the plasma rest frame. Jet structures are found to be mainly thermal and magnetic pressure-balance structures, notwithstanding that the dynamic pressure dominates by far. Although the jet is super-magnetosonic in the Earth's frame of reference, it is sub-magnetosonic with respect to the plasma ahead. Consequently, we find no fast shock. Instead, we find some evidence for (a series of) jets pushing ambient plasma out of their way, thereby stirring the magnetosheath and causing anomalous sunward flows in the subsolar magnetosheath. Furthermore, we find that jets modify the magnetic field in the magnetosheath, aligning it with their propagation direction.

1 Introduction

Jets in the magnetosheath, also called fast plasmoids, are transient localized enhancements in dynamic pressure [e.g., *Němeček et al.*, 1998; *Savin et al.*, 2008; *Karlsson et al.*, 2012], typically caused by increases in plasma velocity. Statistical studies have shown that jets occur more often downstream of the quasi-parallel bow shock [*Archer and Horbury*, 2013; *Plaschke et al.*, 2013]. Thus, the occurrence of jets in the subsolar magnetosheath is primarily controlled by the cone angle of the interplanetary magnetic field (IMF): stable, low IMF cone angle conditions being favorable for jet occurrence. Other solar wind parameters do not seem to have a major influence on the appearance of jets. The jets are associated with slightly larger solar wind velocities, magnetosonic Mach numbers, and IMF strength, but lower solar wind densities. Jet occurrence is, in general, not noticeably enhanced by variations in the IMF or in other solar wind parameters [*Plaschke et al.*, 2013].

Nevertheless, jets are expected to occur and have been observed as a consequence of IMF discontinuities [e.g., *Dmitriev and Suvorova*, 2012; *Archer et al.*, 2012]: Most trivially, the motion of the whole magnetosheath region due to changes in IMF may result in spacecraft observations of transient dynamic pressure changes [*Sibeck and Gosling*, 1996; *Sibeck et al.*, 2000], although no true jets are created thereby. Those may be generated by interaction of IMF discontinuities with the bow shock or with reflected ions in the upstream foreshock region, causing density enhancements and strong boundary-tangential flows in the magnetosheath [*Lin et al.*, 1996a,b; *Lin*, 1997; *Omidi and Sibeck*, 2007]. Also hot flow anomalies that may result from IMF discontinuities have been associated with jets in the magnetosheath [e.g., *Savin et al.*, 2012; *Archer et al.*, 2014]. Overall, however, jets associated with discontinuities have been shown to constitute a minority [*Archer and Horbury*, 2013; *Hietala and Plaschke*, 2013].

A relatively large majority of jets is observed downstream of the quasi-parallel bow shock, in the absence of IMF discontinuities. It is suggested that these jets are generated at undulations or ripples of the bow shock, where the solar wind plasma is compressed, but less decelerated and thermalized when passing through inclined shock surfaces [*Hietala et al.*, 2009, 2012; *Hietala and Plaschke*, 2013]. Such undulations are inherent to the quasi-parallel shock; they are a consequence of the formation and reformation of the shock as steepened foreshock structures merge with it [*Schwartz and Burgess*, 1991; *Omidi et al.*, 2005; *Blanco-Cano et al.*, 2006a,b, 2009].

In comparison with the ambient magnetosheath plasma, jets typically feature (much) larger velocities, enhanced densities, as well as lower and more isotropic temperatures [*Savin et al.*, 2008; *Hietala et al.*, 2009; *Amata et al.*, 2011; *Archer et al.*, 2012; *Plaschke et al.*, 2013]. Unlike the region downstream of the quasi-perpendicular shock where plasma has a higher temperature perpendicular to the magnetic field, downstream of the quasi-parallel shock temperatures are usually more isotropic anyway [*Ellacott and Wilkinson*, 2007]. Within jets, the plasma is almost always super-Alfvénic and a non-negligible fraction of jets feature even super-magnetosonic plasma speeds in the observing spacecraft's or Earth's frame of reference [*Plaschke et al.*, 2013], for which a secondary shock in the sheath closer to the magnetopause is expected [e.g., *Hietala et al.*, 2012; *Karimabadi et al.*, 2014].

Jets link processes at the bow shock and in the upstream foreshock region with the magnetopause [*Savin et al.*, 2012]. Upon impact, jets can generate large but localized magnetopause indentations [*Shue et al.*, 2009; *Amata et al.*, 2011], launch (standing) magnetopause surface waves and inner-magnetospheric compressional fluctuations [*Glassmeier and Heppner*, 1992; *Plaschke et al.*, 2009; *Plaschke and Glassmeier*, 2011; *Archer et al.*, 2013a,b], or possibly trigger localized magnetopause reconnection [*Hietala et al.*, 2012]. Consequently, drift paths of radiation belt electrons [*Elkington et al.*, 2003; *Turner et al.*, 2012], ionospheric convection patterns, and ground magnetic fields [*Hietala et al.*, 2012; *Dmitriev and Suvorova*, 2012; *Archer et al.*, 2013b] may be affected. Recent results by *Han et al.* [2017] even suggest a possible link between diffuse dayside (throat) aurora observations and jets impacting the dayside magnetopause.

The severity of jet impacts should scale with their size. Distributions of scales sizes parallel and perpendicular to the jet's direction of propagation have been found to be well-modeled by exponential functions with characteristic scales of 0.71 R_E (parallel) and 1.34 R_E (perpendicular), respectively [*Plaschke et al.*, 2016a]. Here, R_E denotes the Earth's radius. The corresponding median duration of a jet is approximately 30 s [*Plaschke et al.*, 2013]. On average, jets are observed every 67 min (21 min) by single spacecraft in the subsolar magnetosheath, near the magnetopause, in general (under low IMF cone angle conditions: $< 30°$). Due to the limited size of jets, it is obvious that many of them remain undetected by single spacecraft. Correspondingly, impact rates of jets onto the subsolar magnetopause should be much higher. As calculated by *Plaschke et al.* [2016a], large scale jets alone with cross-sectional diameters $> 2\,R_E$ impact the subsolar magnetopause every 21 min (6 min under low IMF cone angle conditions), on average. Hence, jet impacts are very frequent.

Despite this fact, little attention has been paid so far to the internal structure of jets, which should be of importance with respect to their interaction with the ambient plasma and with the magnetopause upon impact. The reason for this lack of attention might have been the limited time resolution of plasma moments of available spacecraft for highly transient phenomena.

The four Magnetospheric Multiscale (MMS) spacecraft, launched in March 2015, provide us with an excellent opportunity to have a closer look. Within burst data intervals, MMS fields and particle measurements are available with unprecedented time resolution [*Torbert et al.*, 2016; *Pollock et al.*, 2016], which is required, for instance, to capture rapid variations in plasma parameters. During their first science phase (1a), the MMS spacecraft were regularly traversing the dayside subsolar magnetosheath, flying in tight tetrahedral configuration with spacecraft separations on the order of 10 to 100 km [*Burch et al.*, 2016]. The high time resolution and spacecraft configuration allow us to use timing techniques in order to ascertain how jet substructures such as current sheets or wave phase fronts, if present, move inside the jet with respect to the plasma. In this paper, we pay particular attention to one jet out of a series that occurred on 27 December 2015, for which burst data are available, and focus on the internal magnetic field structure, its relation with the plasma velocity, and the motion of structures with respect to the jet and ambient magnetosheath plasmas.

2 Observations

2.1 Upstream Conditions

We focus on the interval between 05:25 and 07:00 UT on 27 December 2015. MMS1 fluxgate magnetometer (FGM) measurements [*Russell et al.*, 2016], IMF measurements from NASA's OMNI high resolution data set [*King and Papitashvili*, 2005], and magnetic field measurements by the Geotail spacecraft are shown in the top three panels (a) to (c) of Figure 1 in Geocentric Solar Ecliptic (GSE) coordinates. At 06:00 UT, the MMS1 spacecraft was located at (11.1, −3.7, −1.1) R_E in GSE, i.e., in the subsolar magnetosheath, slightly towards dawn. Geotail, instead, was observing the solar wind; it was located in the dusk sector at (6.7, 29.0, 3.8) R_E. The positions of the spacecraft are illustrated in Figure 2. The OMNI data correspond to Wind and ACE data that are taken near the L1 point and are propagated to the bow shock nose.

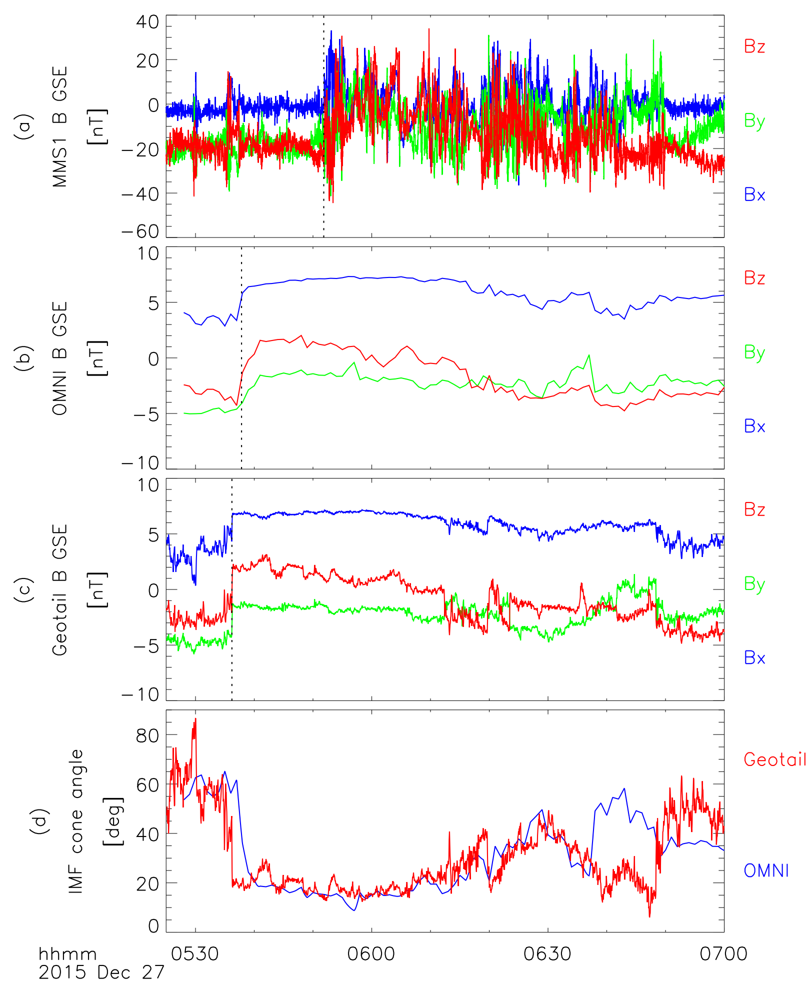

Figure 1. Magnetic field measurements in the solar wind and in the magnetosheath. From top to bottom: (a) MMS1 FGM magnetosheath observations, (b) OMNI IMF data, (c) Geotail IMF data, (d) IMF cone angle from OMNI (blue) and Geotail (red). IMF discontinuity is marked by dotted lines.

As can be seen in panel (a) of Figure 1, the MMS1 magnetic field measurements are relatively calm until about 05:51:50 UT (marked by dotted line). From this point on, major fluctuations are observed until approximately 06:50:00 UT. The fluctuations are typical of the magnetosheath downstream of the quasi-parallel shock. Indeed, a major change (discontinuity) in the IMF is observed in the OMNI data at 05:37:50 UT and in the Geotail data at 05:36:12 UT; both times are also marked by dotted lines in panels (b) and (c), respectively. As shown in panel (d), this discontinuity drastically lowers the IMF cone angle changing the character of the subsolar bow shock from quasi-perpendicular to quasi-parallel. The normal direction of the discontinuity is computed by minimum variance analysis of the OMNI magnetic field data. We obtain: $\vec{n}_{\mathrm{D}} = (-0.36, -0.69, 0.63)$ in GSE. A similar normal vector of $(-0.36, -0.64, 0.67)$ is obtained by taking the cross product of the Geotail-measured magnetic field directions before and after 05:36:12 UT. Minimum variance directions obtained from Geotail data support these results, despite them being associated with higher uncertainties (lower intermediate to low eigenvalue ratios).

Due to the large inclination of $\vec{n}_{\mathrm{D}}$ with respect to the GSE x-direction and the distant position of Geotail, we expect and, indeed, find a significant time delay between the discontinuity observation by Geotail at 05:36:12 UT and the time from which the change in bow shock character affects the magnetosheath observed by MMS1 at 05:51:50 UT (see Figure 2).

The end of the fluctuation interval at 06:50:00 UT nearly corresponds with the end of the low cone angle interval as seen by Geotail, at 06:48:23 UT. In the OMNI data, this cone angle change is predicted to arrive earlier at the bow shock nose, at around 06:37:30 UT. The mean solar wind speed and proton density as given by the OMNI data set between 05:37:50 UT and 06:37:30 UT are $(530 \pm 5)\,\mathrm{km/s}$ and $(2.9 \pm 0.3)\,\mathrm{cm}^{-3}$.

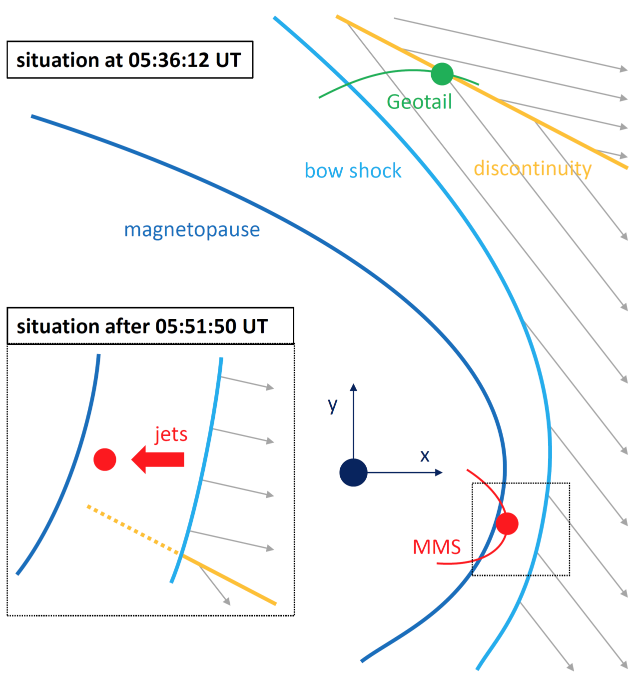

Figure 2. Illustration of the positions of the Geotail and MMS spacecraft as well as the IMF discontinuity at 05:36:12 UT in the GSE x-y-plane. Close-up of the situation at the MMS spacecraft after 05:51:50 UT, when they are positioned downstream of the quasi-parallel shock.

2.2 MMS Downstream of the Quasi-Parallel Shock

MMS1 magnetosheath observations during the interval downstream of the quasi-parallel bow shock (interval of interest) are shown in Figure 3. The top panels (a) and (b) show the FGM-measured magnetic field $\vec{B}$ in GSE and its modulus $|\vec{B}|$. These are 16 Hz fast survey measurements, smoothed by computing a running average over 4.5 s in order to adapt them to the sampling rate of the fast plasma instrument (FPI) data in fast survey mode [*Pollock et al.*, 2016], shown in panels (c) to (g). They show the ion omni-directional differential energy flux, the ion velocity $\vec{V}$ in GSE, the ion density N, the parallel and perpendicular ion temperatures $T_{\|}$ and $T_{\perp}$, and the dynamic pressure using only the x-component of the velocity $P_{\mathrm{dyn},x} = NmV_x^2$. Here m is the proton mass.

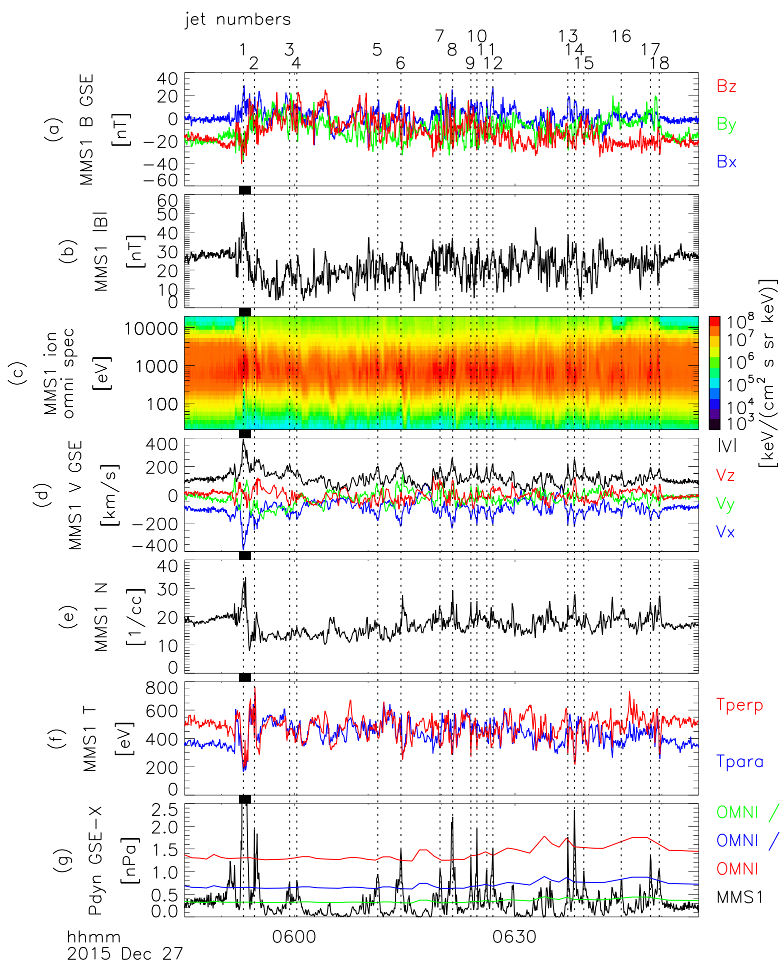

Figure 3. MMS1 magnetosheath measurements in the interval of interest downstream of the quasi-parallel shock. From top to bottom: FGM observations of (a) $\vec{B}$ in GSE, (b) $|\vec{B}|$, and FPI measurements of (c) ion omni-directional differential energy flux, (d) ion velocity $\vec{V}$, (e) ion density N, (f) ion parallel and perpendicular temperatures $T_{\|}$ and $T_{\perp}$ in blue and red, and (g) dynamic pressure $P_{\mathrm{dyn},x} = NmV_x^2$ in black and solar wind dynamic pressures as given by the OMNI data set in red (half and one quarter thereof in blue and green). The dynamic pressure maximum at 05:53:01 UT reaches 7.9 nPa (outside the plot range). The 18 jets identified between 05:51:50 and 06:50:00 UT are marked with dotted vertical lines and numbered at the top of the figure. The black bars between panels depict the burst data interval shown in subsequent figures, between 05:52:25 and 05:54:00 UT.

As evidenced by the high ion densities N in comparison to the solar wind (panel e) and the characteristic ion energy fluxes (panel c), MMS was in the magnetosheath over the entire interval of interest. The velocity data in panel (d) exhibits a series of large transient increases, particularly in negative V_x and correspondingly in $|\vec{V}|$. These increases are magnetosheath high-speed jets, as can be seen in the dynamic pressure data shown in panel (g). In that panel, the solar wind dynamic pressure as well as half and one quarter of it are shown in red, blue, and green, respectively. We define a jet by the ratio between the magnetosheath and solar wind dynamic pressures: That ratio should surpass 1/2, and adjacent intervals where that ratio exceeds 1/4 comprise the jet intervals [*Plaschke et al.*, 2013]. With this definition, there are 18 jets in the interval of interest between 05:51:50 and 06:50:00 UT.

By using the ratio of dynamic pressures for jet identification, we intend to avoid the selection of directly driven, global magnetosheath dynamic pressure enhancements, which are caused merely by increases in solar wind dynamic pressure. It should be noted, however, that the OMNI data cannot resolve well any short term variations in solar wind dynamic pressure, which could potentially be identified as jets. Hence, we also check the (less accurate but more frequent) Geotail plasma data for short term dynamic pressure variations. Within the low cone angle interval (between 05:36:12 and 06:48:23 UT), we find variation amplitudes to be (significantly) lower than 100% of the mean dynamic pressure, while our definition of jets requires higher amplitudes for jet identification (at least 100%). This result indicates that none of the 18 jets identified in this this study may be explained just by solar wind dynamic pressure increases.

Within each of the jet intervals, we search for the maximum in dynamic pressure ratio. These maxima are marked with dotted lines in Figure 3. The positions of these lines obviously correspond very well with enhancements in negative V_x and $|\vec{V}|$, as expected. As can be seen in panel (e), the majority of jets is associated with (slight) density increases, although sometimes these increases do not stand out from the overall density fluctuation level. This observation is in agreement with *Archer and Horbury* [2013], who find jets to be associated with a range of density variations (positive and negative), tending towards density increases rather than decreases. Similarly, we see jets tending to but not always being associated with temperature decreases (panel f) and magnetic field increases (panel b).

We may check to which extent maxima in $-V_x$, N, $|\vec{B}|$ or minima in T correspond to increases in dynamic pressure. Obviously, the correspondence is excellent with respect to $-V_x$. All maxima in $-V_x$ are associated with increases in dynamic pressure $P_{\mathrm{dyn},x}$, and the correlation coefficient between V_x^2 and $P_{\mathrm{dyn},x}$ is 0.96. Hence, the dynamic pressure is strongly velocity dominated, since the correlation coefficient between N and $P_{\mathrm{dyn},x}$ is only 0.58. Nevertheless, stronger maxima in N also generally coincide with maxima in $P_{\mathrm{dyn},x}$. This relationship is far less obvious when checking $T_\perp$ or $T_\parallel$ minima or $|\vec{B}|$ maxima against $P_{\mathrm{dyn},x}$ maxima. Clearly, there are many transient enhancements $|\vec{B}|$ that are not associated with particular enhancements in $-V_x$ or $P_{\mathrm{dyn},x}$. Interestingly, the x-component of the magnetic field (B_x) seems to be much closer associated with the occurrence of jets. That component is shown in blue in panel (a). The correlation coefficients of B_x and $|\vec{B}|$ with V_x are -0.52 and -0.29, respectively. Hence, B_x is more similar to $-V_x$ than $|\vec{B}|$. Note that B_y and B_z are also, to some extent, associated with $-V_y$ and $-V_z$, respectively, as can be seen in Table 1, which shows an overview of correlation coefficients.

2.3 Leading Jet Observations

MMS burst observations are only available for the leading jet number 1, enabling us to take advantage of the high time-resolution of the MMS measurements (burst sampling period of FGM: 8 ms, FPI ion moments: 150 ms). These data are shown in Figure

Table 1. Correlation coefficients pertaining to different quantity pairs: Time series of quantities in the interval of interest between 05:51:50 and 06:50:00 UT were cross-correlated.

	$P_{\text{dyn},x}$	V_x	V_y	V_z
V_x^2	0.96	-0.87	0.16	0.10
N	0.58	-0.44	0.33	0.24
$T_\parallel$	-0.37	0.13	-0.31	-0.19
$T_\perp$	-0.46	0.37	-0.26	-0.12
B_x	0.39	-0.52	-0.16	0.11
B_y	-0.17	0.07	-0.48	0.22
B_z	-0.16	0.04	-0.16	-0.43
$\lvert\vec{B}\rvert$	0.38	-0.29	0.33	0.25

4. From top to bottom, the figure shows $\vec{B}$ from MMS1, the current density $\vec{J}$ determined by the four-spacecraft curlometer method [e.g., *Dunlop et al.*, 2002], MMS1 FPI ion omni-directional differential energy flux, $\vec{V}$, N, $T_\parallel$, $T_\perp$, plasma beta, $P_{\text{dyn},x}$, and the local magnetosonic Mach number M_{ms}. From the figure it is immediately visible that the internal structure of this leading jet is very rich.

The magnetic field (panel a) exhibits numerous fluctuations. Between 05:52:39 and 05:52:44 UT compressional quasi-periodic variations are observed that are associated with fluctuating current densities (panel b). Major rotations in the magnetic field are observed around 05:52:50 UT, between approximately 05:53:18 and 05:53:28 UT, and after 05:53:38 UT; all of these rotations also show up in the current density data. Furthermore, the magnetic fields are different at the beginning and the end of the interval. At the beginning, at 05:52:34 UT, $\vec{B} = (6, -28, -16)\,\text{nT}$, and at the end, at 05:53:53 UT, $\vec{B} = (24, 1, 15)\,\text{nT}$. So the jet marks a transition from a mostly $-y$-aligned field to more radially x-aligned magnetic field. Note that B_x only becomes the dominant component at the very end of the burst data interval. Hence, over larger parts of that interval $(B_y^2+B_z^2)^{1/2}$ is larger than B_x. The measurements in $|\vec{B}|$ range from 7 to 54 nT, showing the highly compressional nature of the variations, even within such a short interval.

Variations are also seen in the temperature (panel f) and, more clearly, in the density data (panel e). Variations in $T_\perp$ reach 570 eV/s, and those in N reach $34\,\text{cm}^{-3}/\text{s}$ at 05:53:38 UT. At 05:53:20 UT the density increases by $25\,\text{cm}^{-3}$ in just 1.65 s, and at 05:53:24 UT a drop in density is observed of over $20\,\text{cm}^{-3}$ in 1.2 s. Clearly, these large gradients in density and temperature could not be observed without the high time-resolution of the MMS measurements. Consequently, the maximum dynamic pressure calculated from the GSE x-component of the velocity associated with jet number 1 is 11.3 nPa (at 05:53:00), based on burst mode observations (Figure 4 panel h) - much higher than 7.9 nPa as determined from fast survey data (Figure 3 panel g).

Interestingly, even at the level of substructures of a jet, there is a correspondence between variations in velocity and magnetic field. This is highlighted by the black vertical dashed lines in panels (a) and (d) of Figure 4. The lines coincide with local maxima in $-V_x$ at 05:52:52, 05:53:00, 05:53:13, 05:53:20, 05:53:28, and 05:53:37 UT. As can be seen in panel (a), they also coincide with local maxima in B_x. The correlation coefficient between B_x and V_x for the burst data interval is, however, low: -0.22. Between B_y and V_y as well as B_z and V_z we also find anti-correlated behavior with coefficients of -0.14 and -0.76, respectively, the B_z to V_z anti-correlation being remarkably strong (compare with Table 1 for the entire interval of interest).

An interesting feature of this particular jet can be seen in panel (i) of Figure 4. The local magnetosonic Mach number $M_{\rm ms}$ in the spacecraft frame of reference exceeds 1 over large parts of the jet interval. Hence, this jet belongs to the subset of super-magnetosonic jets that are observed in the subsolar magnetosheath [e.g., *Savin et al.*, 2011; *Hietala et al.*, 2012; *Plaschke et al.*, 2013]. The 8 instances where $M_{\rm ms} = 1$ are marked in Figure 4 by red dotted lines; they are numbered with letters in the bottom of panel (i). Mach 1 instances A, D, E, and F are associated with local increases in temperature; larger density variations are seen at instances A, B, and F. However, there are also density variations of equal or larger scale that are not associated with $M_{\rm ms} = 1$. Instances of Mach 1 are more distinctly reflected in the current density $\vec{J}$. All but instances D and E (very short excursion below $M_{\rm ms} = 1$) are at or adjacent to noticeable current density enhancements. In order to investigate the nature of these current density enhancements and corresponding magnetic structures, we analyze their propagation speeds with respect to the jet and ambient magnetosheath plasmas and compare them to the characteristic plasma speeds in the following sections.

3 Timing Analysis of Magnetic Structures

The motion of jets is usually defined by the motion of the ions, here specifically in the GSE x-direction, which corresponds to the main ion velocity direction. This ion motion, however, is not necessarily coincident with the motion of structures (current sheets) or waves (wave fronts) that manifest themselves as fluctuations of the magnetic field.

To obtain the velocity $\vec{V}_{\rm s}$ of structures/fluctuations in the magnetic field, and thereby the propagation velocity of waves and/or current sheets, we perform a timing analysis with the method detailed in *Plaschke et al.* [2016b], using 3 s long sliding intervals. This interval length allows for a good time resolution of $\vec{V}_{\rm s}$ while keeping its noise low. Magnetic field data $\vec{B}$ from each 3 s long interval measured by MMS 2, 3, and 4 are compared with data from MMS 1, from an equally long interval (3 s), time shifted by τ. The averages of the components are subtracted from the magnetic field data, yielding modified vector time series $\tilde{\vec{B}}_1$, $\tilde{\vec{B}}_2$, $\tilde{\vec{B}}_3$, and $\tilde{\vec{B}}_4$ for MMS 1, 2, 3, and 4. For each spacecraft pair MMS 1 and 2, 1 and 3, and 1 and 4, we compute the cross-correlation $P(\tau)$, for instance [Equation 2 in *Plaschke et al.*, 2016b]:

$$P_{12}(\tau) = \frac{\sum_t \left(\tilde{\vec{B}}_1(t+\tau)\cdot\tilde{\vec{B}}_2(t)\right)}{\sqrt{\left(\sum_t \tilde{\vec{B}}_1^2(t+\tau)\right)\left(\sum_t \tilde{\vec{B}}_2^2(t)\right)}} \quad (1)$$

P_{12}, P_{13}, and P_{14} are computed for each possible value of τ, which ranges between ± 2 s in steps of $\Delta\tau = (1/128)$ s, which is the burst FGM data sampling period. By using $\tilde{\vec{B}}$ instead of $\vec{B}$, we ensure that magnetic field fluctuations in all directions contribute equally to the cross-correlations P_{12}, P_{13}, and P_{14}. Otherwise, they would be most sensitive to compressional magnetic field fluctuations, directed along the magnetic field.

The maxima in $P_{12}(\tau)$, $P_{13}(\tau)$, and $P_{14}(\tau)$ are reached for certain values of τ, which we denote as lag times τ_{12}, τ_{13}, and τ_{14}. From the leading jet observations, we obtain absolute lag times between 0 and 0.24 s, and an average absolute lag time of 0.076 s. Based on the lag times, we can compute velocities and propagation directions $\vec{V}_{\rm s}$ of the structures via [see *Harvey*, 1998]:

$$\mathbf{R}\cdot\vec{V}_{\rm s}/|\vec{V}_{\rm s}|^2 = \vec{\tau} \quad (2)$$

Here, the matrix $\mathbf{R} = (\vec{r}_1 - \vec{r}_2, \vec{r}_1 - \vec{r}_3, \vec{r}_1 - \vec{r}_4)^{\rm T}$ contains the vectors pointing between the respective spacecraft and the vector $\vec{\tau}$ is defined as: $\vec{\tau} = (\tau_{12}, \tau_{13}, \tau_{14})^{\rm T}$. The structure velocity $\vec{V}_{\rm s}$ is shown in panel (b) of Figure 5. It is important to note that the direction of $\vec{V}_{\rm s}$ is the normal direction of current sheets or wave fronts passing over the spacecraft configuration, and its absolute value is the velocity of those sheets/fronts along their normal direction.

By using the timing analysis, we implicitly assume features in the magnetic field to be well represented by plane wave fronts (planar assumption) over the size of the spacecraft configuration: Inter-spacecraft distances ranged between 31.3 and 38.4 km at 05:53:00 UT. Furthermore, the tetrahedral spacecraft configuration was well-satisfied: The geometric factor is $Q_{\mathrm{GM}} = 2.96$ for the leading jet interval [*Robert et al.*, 1998].

All the maxima of the cross-correlation functions P (Equation 1) are above 0.78 within the jet interval. The maximal angular uncertainty of the velocity computations can be estimated with Equation (1) of *Plaschke et al.* [2016b]: $\arcsin(V_\mathrm{s}\,\Delta t/s)$, where $V_\mathrm{s} \leq 400\,\mathrm{km/s}$ is the structure velocity, Δt is the error in timing, which we assume to be the burst data sampling period and resolution of τ of $\Delta\tau = (1/128)\,\mathrm{s}$, and $s \approx 35\,\mathrm{km}$ is a measure of the spacecraft separation distance. With these numbers, we obtain an upper limit for the angular uncertainty of approximately 5°. An upper limit of the error in velocity ΔV_s can be estimated via:

$$\Delta V_\mathrm{s} = V_\mathrm{s}^2\,\Delta t/s \tag{3}$$

We obtain $\Delta V_\mathrm{s} \leq 37\,\mathrm{km/s}$ assuming $V_\mathrm{s} \leq 400\,\mathrm{km/s}$. As can be seen in panel (f) of Figure 5, ΔV_s is time-dependent (as are V_s and, in principle, s) and usually much smaller than 37 km/s.

The structure velocity $\vec{V}_\mathrm{s}$ can be split into the magnetic field-parallel component $V_{\mathrm{s}\|}$ (shown in red panel c of Figure 5) and the part of $\vec{V}_\mathrm{s}$ perpendicular to $\vec{B}$: $V_{\mathrm{s}\perp}$ (red line, panel d). Both panels (c) and (d) show also the ion velocity components in the same directions: $V_\|$ and $V_\perp$ in blue. It is apparent that structures in the magnetic field do not seem to have a large velocity component parallel to the field. $V_\|$ is (much) larger than $V_{\mathrm{s}\|}$ throughout the jet interval. This indicates that the normal directions $\vec{V}_\mathrm{s}/|\vec{V}_\mathrm{s}|$ of the structures, wave fronts, or current sheets are oriented primarily perpendicular to the local magnetic fields. This can be understood, e.g., in terms of current sheets at tangential discontinuities or at rotational discontinuities with small normal magnetic fields.

In stark contrast therewith, the structure and ion velocities along $\vec{V}_{\mathrm{s}\perp}$ coincide very well (see panel d of Figure 5). This indicates that the current sheets or structures within the jet are mainly (to a first order) convected with the plasma, as illustrated in Figure 6. This statement does not mean, that the plasma is absolutely dominating the motion of fields and structures, as evidenced by the plasma beta inside the jet shown in panel (g) of Figure 4. The plasma beta within the jet and, in particular, at larger current sheets is around or not much larger than unity. The magnetic field, hence, should still have the ability to influence the motion of the plasma.

In detail, however, the ion velocity does differ sometimes within the jet from the structure velocity in the direction normal to structure fronts or current sheets. Panel (b) of Figure 7 depicts this velocity difference $V_{\mathrm{diff}} = (\vec{V} - \vec{V}_\mathrm{s}) \cdot (\vec{V}_\mathrm{s}/|\vec{V}_\mathrm{s}|)$ in black. The uncertainty in this velocity difference (due to our estimated structure velocities) is shown in the shaded yellow areas as $V_{\mathrm{diff}} \pm \Delta V_\mathrm{s}$. Times at which V_{diff} deviates less than ΔV_s from 0 km/s are indicated by a red bar at the bottom of panel (b) and at the top of panel (c). At those instances, structures in the magnetic field move at the same speed as the ambient plasma and current sheets are likely to be tangential discontinuities, as no plasma flow across them is detected.

When V_{diff} is non-vanishing, then we may check if it coincides with the Alfvén velocity $V_{\mathrm{A}n}$ normal to structures/wave fronts, indicating the presence of a rotational discontinuity, an Alfvén wave, or (in theory) an intermediate shock (unlikely to be stable). $V_{\mathrm{A}n}$ with its sign adapted to the sign of V_{diff} is shown in green in panel (b) of Figure 7. Times at which $\pm V_{\mathrm{A}n}$ agrees with V_{diff} within the uncertainty ΔV_s are indicated by a green bar at the bottom of the panel.

To check if the V_{diff} excursions and corresponding current sheets could be associated with shocks, we check whether these current sheets/structures move with the velocities:

$$V_{\mathrm{fast/slow}}^2 = \frac{1}{2}\left((C_{\mathrm{s}}^2 + V_{\mathrm{A}}^2) \pm \sqrt{(C_{\mathrm{s}}^2 + V_{\mathrm{A}}^2)^2 - 4C_{\mathrm{s}}^2 V_{\mathrm{A}}^2 \cos^2\theta_{Bn}}\right) \tag{4}$$

with respect to the upstream flow. Here, θ_{Bn} is the angle between the structure normal vectors $\vec{V}_{\mathrm{s}}/|\vec{V}_{\mathrm{s}}|$ and the magnetic field directions $\vec{B}/|\vec{B}|$. $V_{\mathrm{fast/slow}}$ are shown in light and dark blue, respectively, in panel (c) of Figure 7. The upstream plasma flow has to be measured before/after the current sheets if V_{diff} is lower/higher than zero, as the plasma is found to move slower/faster than the sheets. Hence, we recompute V_{diff} using ion velocity measurements time-shifted by ± 2 s; this quantity ($|V_{\mathrm{diff,up}}|$) is shown in black in panel (c) of Figure 7. The yellow area around it depicts again the associated uncertainty ΔV_{s}. Times at which $|V_{\mathrm{diff,up}}| \approx V_{\mathrm{slow}}$ (approximately equal taking into account the uncertainty ΔV_{s}) are marked by a blue bar at the top of panel (c). Just based on the velocity, they could indicate times of slow shocks, though their appearance would seem to be unlikely. Times of $|V_{\mathrm{diff,up}}| \approx V_{\mathrm{fast}}$ would suggest the presence of a fast shock.

4 Discussion

4.1 Motion of Structures and Current Sheets

For the subsequent discussion, we select a few times of interest (TOIs) within jet number 1, at which prominent current sheets or plasma flows normal to those sheets/structures were observed. These times of interest are marked with black dotted lines in Figure 7 and are numbered with roman numerals at the top of that figure. The times are: 05:52:48.8, 05:52:51.1, 05:53:21.5, 05:53:25.0, 05:53:29.2, 05:53:36.7, and 05:53:38.4 UT. Note that the findings and discussions on the TOIs are also summarized in Table 2.

As can be seen in panel (c) of Figure 7, V_{fast} is always much larger than $|V_{\mathrm{diff,up}}|$. Hence, there is no fast shock within jet number 1. The fast jet plasma is not super-magnetosonic with respect to the plasma ahead, so that a fast shock could develop inside the jet. Note, however, that the ion velocity becomes super-magnetosonic in the frame of reference of the spacecraft and therefore likely the magnetopause (see panel i of Figure 4), with which the jet is destined to collide given its direction of motion. Thus, at some point closer to the magnetopause, a shock may develop as seen, for instance, by *Hietala et al.* [2012], due to the plasma ahead of the jet slowing down when approaching the magnetopause boundary. Note that the plasma inside the jet is super-magnetosonic not only because the ion velocity is larger, but also because the magnetosonic velocity V_{ms} is lower than in the ambient magnetosheath (see panel d of Figure 7). Jet plasma appears to be more similar to solar wind plasma, i.e., less thermalized with respect to the magnetosheath plasma surrounding it [e.g., *Plaschke et al.*, 2013].

During 37% of the time interval of jet number 1, magnetic field structures are simply propagating with the plasma, without any plasma flow normal to the structures when taking into account the uncertainty ΔV_{s}, illustrated by the red bars in panels (b) and (c) of Figure 7. This holds in particular for the current sheet at TOI I, at the beginning of the jet, which may be characterized as tangential discontinuity.

At TOI II, instead, $V_{\mathrm{diff}} > 0$. Hence, the current sheet observed at that time is actually overtaken by the plasma while both (plasma and current sheet) propagate toward the magnetopause. In other words, the current sheet propagates backward, away from the magnetopause in the frame of reference of the ambient plasma, but is convected towards the magnetopause by the flow. We find $V_{\mathrm{diff}} \approx V_{\mathrm{A}n}$ (within the margin of error ΔV_{s}), suggesting that the current sheet could be a rotational discontinuity or an intermediate shock. The latter would exhibit a change in thermal and magnetic pressures across the current sheet. The question whether such pressure changes are observed is addressed below.

In general, at the beginning of the jet until about 05:52:55 UT and at the end of the jet after about 05:53:30 UT, magnetic field structures appear to be propagating backward, i.e., toward the bow shock and against the flow in the plasma's frame of reference ($V_{\text{diff}} > 0$). In the central part of the jet, instead, the magnetic field structures mostly overtake the plasma, i.e., structures move toward the magnetopause faster than the plasma ($V_{\text{diff}} < 0$).

Larger deviations of V_{diff} from zero are seen between 05:52:56 and 05:53:15 UT, and at TOIs III to VI. The interval (between 05:52:56 and 05:53:15 UT) does not encompass any significant current density enhancements. This could suggest that we are seeing waves propagating in the direction of plasma motion with excess velocity relative to that motion. The velocities V_{diff} only reach values up to about 70 km/s, which is smaller than the sound, Alfvén, and magnetosonic speeds C_{s}, V_{A}, and $V_{\text{ms}} = (V_{\text{A}}^2 + C_{\text{s}}^2)^{1/2}$, which are depicted in panel (d) of Figure 7. Note that this observation holds in general, for the entire jet interval, reducing the likelihood of propagating fast magnetosonic or sound waves. The Alfvén velocity normal to the wave fronts $V_{\text{A}n}$ is in general lower than V_{diff}, but often within the uncertainty ΔV_{s} (see panel b of Figure 7), hence, suggesting that waves within the mentioned interval (between 05:52:56 and 05:53:15 UT) could be Alfvén waves propagating at a large angle to the direction of the ambient magnetic field.

TOIs III and IV are clearly associated with current density enhancements, while TOIs V and VI are not. It is clear that the relatively large V_{diff} excludes the possibility of the current sheets at TOIs III and IV to be tangential discontinuities. Furthermore, from the four TOIs III to VI, only at TOI VI $V_{\text{diff}} \approx V_{\text{A}n}$ holds, suggesting the presence of an Alfvén wave, as there is no discontinuity at this particular time. Hence, current sheets at TOIs III and IV are probably not rotational discontinuities. This also holds for the current sheet at TOI VII, whose V_{diff} is not that large (in comparison to V_{diff} at TOIs III to VI), though large enough to deviate from zero and from $V_{\text{A}n}$ by more than the uncertainty ΔV_{s}.

Interestingly, the current sheets at TOIs III and VII, propagate with a velocity close to V_{slow} with respect to the upstream plasma, i.e., the ambient plasma that moves towards the sheet. In theory, this fact could be seen as a slight indication in favor of the hypothesis that the current sheets might be slow shocks, without further checking the jump conditions across the current sheet or whether such a shock would actually be stable. We address this hypothesis again below.

4.2 Pressures

Across a shock (unlike across a rotational discontinuity) the thermal pressure should change. We see that density and temperature variations are significant within the leading jet, but also that the two quantities are anti-correlated, moderating variability in the thermal pressure $P_{\text{thermal}} = NT_{\perp}$. It is shown in panel (a) of Figure 8 in blue. P_{thermal} varies between 0.57 and 1.56 nPa. Note that we neglect here the pressure anisotropy and also the electron contribution to the thermal pressure. The latter assumption is justified as $T_{\perp,\text{electrons}}$ is significantly smaller than $T_{\perp,\text{ions}}$ over the leading jet interval, on average by a factor of ~ 7. When calculating the isotropic pressure from both parallel and perpendicular pressures, we see that the difference to P_{thermal} as calculated above is also small, justifying the former assumption: On average, $2T_{\perp} + T_{\parallel}$ differs from $3T_{\perp}$ by less than 5%, as $T_{\parallel}/T_{\perp} \sim 0.86$ (see panel f of Figure 4). Correspondingly, the (average) modification factor to the normal Alfvén velocity $V_{\text{A}n}$ due to the pressure anisotropy $(1 - \mu_0 N(T_{\parallel} - T_{\perp})/B^2)^{1/2}$ is also small: ~ 1.1.

Panel (a) of Figure 8 shows also the magnetic pressure $P_{\text{mag}} = B^2/(2\mu_0)$ in green. P_{thermal} and P_{mag} are clearly anti-correlated, the correlation coefficient being -0.86 after subtracting the linear trends from both quantities. As can be seen, the sum of P_{thermal} and P_{mag} exhibits less variability (panel a). On the scale of panel (b), $P_{\text{thermal}} + P_{\text{mag}}$ is essentially constant. Hence, the substructures seen within the jet are mainly pressure balance structures when taking into account thermal and magnetic pressures. Some major variations in $P_{\text{thermal}} + P_{\text{mag}}$ are seen though at the current sheets at TOIs III and IV.

At TOI III, P_{mag} has a local minimum and P_{thermal} exhibits a decrease. The associated current sheet has been found to propagate faster than the plasma away from the bow shock (negative V_{diff}). Hence, the measurements before/after TOI III correspond to the upstream/downstream side. As can be seen in Figure 8, P_{thermal} is larger upstream than downstream, which contradicts the hypothesis of this current sheet pertaining to a slow shock. At TOI VII, we only observe a local dip in P_{thermal}, embedded in an overall increase (also in P_{mag}), but no jump across the current sheet, which also deviates from expectations with respect to a slow shock.

Such a jump is observed at TOI II. The current sheet observed at that time propagates away from the bow shock slower than the plasma. Hence, measurements before/after TOI II pertain to the downstream/upstream plasma. It is apparent that P_{thermal} increases from the upstream to the downstream side. Furthermore, P_{mag} decreases by the same amount so that sum of the two pressures remains constant. These findings support the hypothesis (but are not at all conclusive evidence) of the current sheet at TOI II pertaining to an intermediate shock, under the assumption of pressure isotropy. When taking into account the small pressure anisotropy that is observed, however, then only the sum of P_{thermal} and P_{mag} need to be continuous over a rotational discontinuity. Hence, at TOI II also the presence of a rotational discontinuity cannot be ruled out.

Over the entire interval of jet number 1, there is a trend for the sum of both P_{thermal} and P_{mag} to decrease, possibly as the jet marks the transition of the magnetosheath downstream of the quasi-perpendicular to the quasi-parallel shock. Adding the dynamic pressure $P_{\text{dyn},x}$ to $P_{\text{thermal}} + P_{\text{mag}}$ yields the red graph in panel (b) of Figure 8. Apparently, the dynamic pressure during the jet interval becomes an order of magnitude larger than the thermal and magnetic pressures. At the beginning and end of the interval, however, $P_{\text{dyn},x} < P_{\text{thermal}} + P_{\text{mag}}$. There the thermal pressure dominates as usual in the subsolar magnetosheath.

This can also be seen in Figure 9, which depicts the same quantities as 8 for the interval of interest, comprising jets 1 to 18. Unfortunately, MMS burst data are only available for jet number 1, making it hard to check whether pressure balance between P_{thermal} and P_{mag} is maintained internally on small time scales within the other jets 2 to 18, as well. Nevertheless, Figure 9 confirms the well-known dominance of the dynamic pressure during jet observations and, furthermore, shows that there is a tendency for jets to coincide with smaller increases in thermal pressure with respect to the ambient sheath plasma, as well.

4.3 Interaction with Ambient Magnetosheath Plasma

We can compare $\vec{V}$ and $\vec{V}_{\text{s}}$ with a reference velocity of plasma moving through the magnetosheath at the location of MMS. As can be seen in panel (d) of Figure 3, the magnetosheath interval of observation downstream of the quasi-parallel shock is characterized by large fluctuations in velocity. The mean velocity during that interval (05:51:50 to 06:50:00 UT) is $(-92.8, -25.2, -4.5)$ km/s in GSE. This can be truly regarded as the average flow velocity at the point of observations, as the mean velocity from the quieter intervals surrounding the interval of interest is basically the same: We average ion velocity measurements from 05:38 to 05:50 UT and from 06:52 to 07:01 UT and obtain $(-96.7, -22.0, 1.7)$ km/s in GSE. The average of the two velocities is $\vec{V}_{\text{ref}} = (-94.7, -23.6, -1.4)$ km/s. We use this as a reference velocity. It is illustrated by black solid lines in Figure 10, which also shows the three components of the ion velocity $\vec{V}$ during the interval of interest.

The differences $(\vec{V}_{\text{ref}} - \vec{V}_{\text{s}}) \cdot (\vec{V}_{\text{s}}/|\vec{V}_{\text{s}}|)$ and $(\vec{V}_{\text{ref}} - \vec{V}) \cdot (\vec{V}/|\vec{V}|)$ are shown in panel (e) of Figure 7. They are (strongly) negative throughout the interval of jet 1. Hence, the

Table 2. Summary of findings and discussions pertaining to TOIs.

TOI	times [UT]	current enhancement	cross-structure flow (plasma/structure faster)	velocity relations	pressure jumps upstream to downstream	possible mode
I	05:52:48.8	yes	no (N/A)	$V_{\text{diff}} \approx 0$	yes, but $P_{\text{thermal}} + P_{\text{mag}}$ constant	tangential discontinuity
II	05:52:51.1	yes	yes (plasma)	$V_{\text{diff}} \approx V_{\text{A}n}$	P_{thermal} increases, P_{mag} decreases, $P_{\text{thermal}} + P_{\text{mag}}$ constant	intermediate shock or rotational discontinuity
N/A	05:52:56 to 05:53:15	no	yes (mostly structures)	$V_{\text{diff}} \geq V_{\text{A}n}$	N/A	Alfvén waves
III	05:53:21.5	yes	yes (structure)	$V_{\text{diff}} > V_{\text{A}n}$, $V_{\text{diff,up}} \approx V_{\text{slow}}$	P_{thermal} decreases	?
IV	05:53:25.0	yes	yes (structure)	$V_{\text{diff}} > V_{\text{A}n}$, $V_{\text{diff,up}} > V_{\text{slow}}$	no	?
V	05:53:29.2	no	yes (structure)	$V_{\text{diff}} > V_{\text{A}n}$, $V_{\text{diff,up}} > V_{\text{slow}}$	no	?
VI	05:53:36.7	no	yes (plasma)	$V_{\text{diff}} \approx V_{\text{A}n}$	no	Alfvén wave
VII	05:53:38.4	yes	yes (plasma)	$V_{\text{diff}} > V_{\text{A}n}$, $V_{\text{diff,up}} \approx V_{\text{slow}}$	no	?

current sheets/structures within the jet and also the jet plasma catch up with the plasma ahead of it in the magnetosheath. If we assume the jet to be impenetrable to the ambient plasma, which is not unreasonable to believe, since we see plasma mainly co-moving with structures perpendicular to $\vec{B}$ (see panel d or Figure 5), even overtaking structures at the beginning of the jet interval ($V_{\mathrm{diff}} > 0$, see panel b of Figure 7), then the plasma ahead of the jet could (i) be accelerated in jet-direction and contribute to that jet or (ii) be pushed out of the region ahead of the jet.

In case (i), we would expect the jet to pick up plasma ahead. Furthermore, the magnetic field and density should become enhanced at the front as a result of a snow plow effect. Jet 1 itself does not seem to exhibit such a behavior. The density is largest in the middle of that jet and there is no distinct front discernible in the jet observations. However, there is an indication that there is an increase in P_{thermal} ahead of jet 1 (see Figure 9), driven by an increase in temperature (see panel f of Figure 3). Note that the correspondence of increased density and velocity in the middle of the jet would be expected if the jet could be defined as a compressional wave traveling through the magnetosheath plasma. However, in this case the temperatures should not drop and the pressure $P_{\mathrm{thermal}} + P_{\mathrm{mag}}$ should maximize within the jet, contrary to observations. This option would also violate the assumption of the jet being impenetrable to ambient plasma.

In case (ii), if the jet were of global scale, i.e., a dynamic pressure enhancement along the former IMF discontinuity [see, *Lin et al.*, 1996a,b], the plasma between the jet and the magnetopause would have to be squeezed out, leading to dominant plasma velocities tangential to any jet front. As can be seen in Figure 5, at the beginning of the jet, the dominant velocity component of $\vec{V}$ is parallel to $\vec{V}_{\mathrm{s}}$, i.e., parallel to the structure-normal direction, in contrast to the expected behavior. Ahead of the jet, however, there is a noticeable increase in $-V_y$ and V_z and a decrease in $-V_x$ ($\vec{V} = (-78, -101, 47)$ km/s at 05:52:30 UT) that could indicate a motion of evasion of that plasma (see Figure 10 just before jet 1). Note that at the beginning of jet number 1, we see $\vec{V}_{\mathrm{s}} = (-121, -90, 57)$ km/s, i.e., $\vec{V}_{\mathrm{s}}/|\vec{V}_{\mathrm{s}}| = (-0.75, -0.56, 0.35)$, which is not very different from the normal vector $\vec{n}_{\mathrm{D}} = (-0.36, -0.69, 0.63)$ of the IMF discontinuity. Similar values of $\vec{V}_{\mathrm{s}}/|\vec{V}_{\mathrm{s}}|$ are also obtained for other instances within jet 1, as can be seen in Figure 5. It is suggested that some of the structures seen within jet 1 pertain to the IMF discontinuity, tilted towards x when passing through the bow shock. As discussed by *Archer et al.* [2012], the IMF discontinuity could also split into smaller entities of high dynamic pressure. In this case, the evasion of plasma ahead of those could also be local and the jet front tangential velocities associated therewith would not have to be large.

Although there are certainly similarities between jet 1 and jets 2 to 18, there are characteristics of jet 1 that make it distinct from the other jets. Jet number 1 has by far the highest dynamic pressure within the interval of interest, and it is linked to the transition from the quasi-perpendicular to the quasi-parallel bow shock. Jets 2 to 18, instead, are rather related to the presence of (not the transition to) the quasi-parallel bow shock; they are possibly generated due to bow shock rippling, as detailed in *Hietala et al.* [2009, 2012]. Downstream of the "steady" quasi-parallel shock, jets of limited scale are expected and, indeed, found to be much more prevalent than large scale jets [*Plaschke et al.*, 2016a].

Correspondingly, if jets push plasma aside when propagating through the magnetosheath, that process should have local character. It should manifest itself in ambient magnetosheath plasma, in the vicinity of jets, being accelerated in perpendicular and opposite directions to the jet's direction of propagation. That ambient plasma should, hence, slow down in its anti-sunward motion, and may even start moving in sunward direction in the Earth's frame of reference, as illustrated in Figure 11. *Karimabadi et al.* [2014] observe this sunward plasma motion in simulations as a reaction to jets penetrating the magnetosheath. As they point out, jets would in that way be stirring the magnetosheath and be a source of additional turbulence.

In agreement with that picture, we see large fluctuations in the ion velocity around the reference velocity $\vec{V}_{\mathrm{ref}}$, as evidenced in Figure 10. Between jet observations that are marked by vertical black dotted lines, $V_x - V_{\mathrm{ref},x}$ is often positive. Hence, ambient plasma is found to move slower there, in the anti-sunward direction, with respect to the plasma motion that is expected at the location of MMS1. At four instances marked by arrows in Figure 10, at 06:17:50, 06:30:49, 06:33:58, and 06:36:22 UT, V_x even turns positive in GSE, indicating sunward magnetosheath plasma motion in the Earth's frame of reference. We interpret this as a possible indication of jets passing by in the vicinity of the MMS spacecraft, and MMS observing the ambient plasma evade the jets.

It should be noted, however, that the observations cannot be regarded as fully conclusive evidence, as the MMS spacecraft configuration is too tight to observe both, the jet (cause) and the sunward moving plasma (effect) outside of the jet's way, at the same time. Hence, it is also possible that the sunward motion of plasma may have been caused by another mechanism. Alternatively, the sunward motion of magnetosheath plasma and the anti-sunward propagation of jets may also be seen as representatives of the tails of the V_x distribution, which is known to be significantly broadened downstream of the quasi-parallel shock in comparison to the quieter magnetosheath downstream of the quasi-perpendicular shock [e.g., *Němeček et al.*, 2000, 2002].

Furthermore, jet 1 and most of the jets 2 to 18 have in common that there is a correspondence between $-V_x$ and B_x, even on a sub-jet level. We suggest this correspondence to be the direct consequence of fast jet plasma moving through slower ambient magnetosheath plasma, as illustrated in Figure 12: To the first order, structures are convected with the jet; the hydrodynamic plasma motion modifies the magnetic field in the vicinity of the jet as indicated by the green line. Thereby, a region in the jet and also behind it should appear, in which the magnetic field is opposed to the jet's flow direction. This is in agreement with our observations of anti-correlation of V_x and B_x, V_y and B_y, and well as V_z and B_z. Note that correlation instead of anti-correlation is expected, if the IMF points in anti-sunward direction at the quasi-parallel bow shock, where jets are generated. Further in agreement with this picture, we observe $V_{\|}$ to dominate over $V_{\perp}$ and $V_{\perp\perp}$ at the end of jet 1, as can be seen in panels (c) to (e) of Figure 5.

With respect to the jets' magnetic field, our observations are also in good agreement with simulation results by *Karimabadi et al.* [2014]. In their simulations, the IMF is nearly radial ahead of the bow shock. Within the magnetosheath, jets are associated with regions of radial magnetic field as well, similar to the upstream field, in contrast to ambient magnetosheath plasma outside of jets.

5 Summary and Conclusions

On 27 December 2015, an IMF discontinuity changed the character of the dayside subsolar terrestrial bow shock from quasi-perpendicular to quasi-parallel. The four MMS spacecraft were located downstream of the bow shock, in the magnetosheath region. They observed a leading jet, associated with the IMF discontinuity and with the change in character of the bow shock, and a subsequent series of jets that appeared downstream of the "steady" quasi-parallel shock. The leading jet was, by far, the strongest, i.e., it exhibited the largest dynamic pressure of $P_{\mathrm{dyn},x} = 11.3\,\mathrm{nPa}$. High time-resolution burst mode measurements are available for this jet. All jets were characterized by a transient increase in $-V_x$ and $P_{\mathrm{dyn},x} = NmV_x^2$, so that $P_{\mathrm{dyn},x}$ in the magnetosheath surpassed half the solar wind's dynamic pressure.

As previously reported, jets tend to be associated with increases in density, magnetic field strength, and temperature, though this correspondence is not one-to-one. Furthermore, we see for the first time $-V_x$, $-V_y$, and $-V_z$ to be correlated with B_x, B_y, and B_z, respectively. This holds also within the leading jet, on a smaller scale substructure level, and confirms earlier simulation results by *Karimabadi et al.* [2014]: Jets' prominent $-V_x$ velocity increases are associated with B_x increases, B_x being the main IMF component. The reason is possibly the high velocity with which jets move through slower ambient magnetosheath plasma, thereby straightening the magnetic field on their way.

Ahead of the jets, the slower ambient plasma needs to be compressed and accelerated in the jets' propagation direction or be pushed aside. We see little indication for the former option. There is, however, some evidence for evasive plasma motion in the ambient magnetosheath ahead of the leading jet and between observations of subsequent jets, in the form of sunward plasma motion even in the Earth's frame of reference. In this case, jets would be stirring the magnetosheath plasma [*Karimabadi et al.*, 2014]. As expected, the long-term average flow velocity at the location of the MMS spacecraft is equal before and after the IMF discontinuity changes the character of the bow shock from quasi-perpendicular to quasi-parallel; the fluctuation level, however, is much higher after.

The plasma ahead of a jet can only evade that jet if information travels faster in the magnetosheath than the jet propagates, i.e., if the jet is sub-magnetosonic in the frame of reference of the ambient magnetosheath. We find the fastest leading jet plasma to be super-magnetosonic in the spacecraft frame of reference, due to increased velocity and lower magnetosonic speed within the jet, plasma there being more similar to the solar wind than the ambient magnetosheath plasma. In the frame of reference of the plasma ahead, the leading jet is not super-magnetosonic. Accordingly, we find no evidence of a fast shock at the beginning of the jet or anywhere within the jet. However, as the jet approaches the magnetopause, a shock might develop as the plasma ahead of the jet slows down [*Hietala et al.*, 2012].

In fact, magnetic field structures/variations due to current sheets or waves within the leading jet are found to move basically at equal speed to the jet plasma. The structure/sheet normals are found to be oriented mainly perpendicular to the local magnetic fields, and their motion is, to the first order, in good agreement with the local plasma velocity. Hence, structures are mainly convected with the jet plasma flow.

In detail, however, there are sometimes small non-vanishing plasma flows across structures/current sheets with velocity differences of less than 100 km/s. These flows are such that the plasma tends to overtake structures at the beginning and end of the leading jet (i.e., structures moving toward the bow shock in the plasma's frame of reference), curiously where the plasma is relatively slow, while structures are found to move faster than the plasma toward the magnetopause in the central part of the jet, where the plasma velocity maximizes. Hence, within the jet, structures propagate forward in the jet's core region, and backward outside of that region.

In general, the leading jet observations reveal that the internal structure of that jet is very rich, exhibiting large amplitude density, temperature, and magnetic field variations over small scales/short periods of time. The density and temperatures are found to be anti-correlated in the jet, which limits the variability in the thermal pressure P_{thermal}. Nevertheless, significant fluctuations are found in P_{thermal} which are essentially compensated by the magnetic pressure P_{mag}. Hence, structures within the leading jet are, to the first order, pressure balance structures, without taking into account the dynamic pressure.

Based on the relative velocities of plasma and structures, it is suggested that two current sheets observed in the front part of the leading jet (at TOIs I and II) could be a tangential discontinuity and an intermediate shock or a rotational discontinuity, respectively, notwithstanding that an intermediate shock may not stable. Other current sheets could not be successfully categorized, as either their propagation speeds and/or the thermal pressure variations across them do not match with expectations. However, other structures not related to significant current density enhancements are observed to move with speeds close to the normal Alfvén velocity, suggesting the presence of Alfvén waves inside the jet (see Table 2 for a summary of the findings).

5.1 Outlook

Revealing the internal structure and inner workings of magnetosheath high-speed jets is a key element to understanding how they can interact with the magnetopause, e.g., in terms of triggering magnetopause reconnection. Clearly, this study can only be regarded as a first step towards a full characterization of the jets' inner structure. First and foremost, the study focuses on a "special" jet that is associated with an IMF discontinuity and a corresponding change in bow shock character. Second, it is a case study, hence, not allowing to draw any general conclusions. More jets need to be studied, in particular of those generated at the "steady" quasi-parallel shock, to investigate whether a common internal structure pattern exists, whether that structure is imposed/created at the bow shock, or to which extend it forms/evolves in the magnetosheath.

Furthermore, this study deals with jets only in the framework of magnetohydrodynamic (MHD) theory. Within the leading jet, proton gyro-scales are mostly under 100 km, which converts to time scales of far less than a second due to the high propagation velocity of the jets. Consequently, most internal structures are (significantly) larger than proton gyro-scales, justifying a posteriori the MHD treatment. Nevertheless, in future studies, structures of kinetic nature need to be addressed as well, possibly uncovering an even richer picture of jets and their role in the overall thermalization process of solar wind plasma at and downstream of the collisionless bow shock.

Acknowledgments

The dedication and expertise of the Magnetopheric MultiScale (MMS) development and operations teams are greatly appreciated. Their work was supported by NASA contract NNG04EB99C. We acknowledge the use of Level 2 burst and fast survey Flux-Gate Magnetometer (FGM) and Fast Plasma Investigation (FPI) data. The FGM and FPI data are stored at the MMS Science Data Center https://lasp.colorado.edu/mms/sdc/ and are publicly available. Fast survey and burst FGM data are based on Analogue Flux-Gate (AFG) and Digital Flux-Gate (DFG) magnetic field measurements, respectively. The Austrian part of the development, operation, and calibration of the DFG was financially supported by rolling grant of the Austrian Academy of Sciences and the Austrian Space Applications Programme with the contract FFG/ASAP-844377. Geotail magnetic field data were provided by T. Nagai through DARTS at the Institute of Space and Astronautical Science, JAXA, Japan. The work of HH was supported by NASA grant NNX17AI45G and contract NAS5-02099. ZV was supported by Austrian FWF grant P 28764-N27. We acknowledge valuable discussions within the International Space Science Institute (ISSI) team called "Jets downstream of collisionless shocks" led by two authors of this paper (FP and HH).

References

Amata, E., S. P. Savin, D. Ambrosino, Y. V. Bogdanova, M. F. Marcucci, S. Romanov, and A. Skalsky (2011), High kinetic energy density jets in the Earth's magnetosheath: A case study, *Planet. Space Sci.*, *59*, 482–494, doi:10.1016/j.pss.2010.07.021.

Archer, M. O., and T. S. Horbury (2013), Magnetosheath dynamic pressure enhancements: occurrence and typical properties, *Ann. Geophys.*, *31*, 319–331, doi:10.5194/angeo-31-319-2013.

Archer, M. O., T. S. Horbury, and J. P. Eastwood (2012), Magnetosheath pressure pulses: Generation downstream of the bow shock from solar wind discontinuities, *J. Geophys. Res.*, *117*, A05228, doi:10.1029/2011JA017468.

Archer, M. O., M. D. Hartinger, and T. S. Horbury (2013a), Magnetospheric ”magic” frequencies as magnetopause surface eigenmodes, *Geophys. Res. Lett.*, *40*, 5003–5008, doi: 10.1002/grl.50979.

Archer, M. O., T. S. Horbury, J. P. Eastwood, J. M. Weygand, and T. K. Yeoman (2013b), Magnetospheric response to magnetosheath pressure pulses: A low-pass filter effect, *J. Geophys. Res.*, *118*, 5454–5466, doi:10.1002/jgra.50519.

Archer, M. O., D. L. Turner, J. P. Eastwood, T. S. Horbury, and S. J. Schwartz (2014), The role of pressure gradients in driving sunward magnetosheath flows and magnetopause motion, *J. Geophys. Res.*, *119*, 8117–8125, doi:10.1002/2014JA020342.

Blanco-Cano, X., N. Omidi, and C. T. Russell (2006a), Macrostructure of collisionless bow shocks: 2. ULF waves in the foreshock and magnetosheath, *J. Geophys. Res.*, *111*(A10), A10205, doi:10.1029/2005JA011421.

Blanco-Cano, X., N. Omidi, and C. T. Russell (2006b), ULF waves and their influence on bow shock and magnetosheath structures, *Adv. Space Res.*, *37*, 1522–1531, doi: 10.1016/j.asr.2005.10.043.

Blanco-Cano, X., N. Omidi, and C. T. Russell (2009), Global hybrid simulations: Foreshock waves and cavitons under radial interplanetary magnetic field geometry, *J. Geophys. Res.*, *114*, A01216, doi:10.1029/2008JA013406.

Burch, J. L., T. E. Moore, R. B. Torbert, and B. L. Giles (2016), Magnetospheric Multiscale Overview and Science Objectives, *Space Sci. Rev.*, *199*(1), 5–21, doi: 10.1007/s11214-015-0164-9.

Dmitriev, A. V., and A. V. Suvorova (2012), Traveling magnetopause distortion related to a large-scale magnetosheath plasma jet: THEMIS and ground-based observations, *J. Geophys. Res.*, *117*, A08217, doi:10.1029/2011JA016861.

Dunlop, M. W., A. Balogh, K.-H. Glassmeier, and P. Robert (2002), Four-point Cluster application of magnetic field analysis tools: The Curlometer, *J. Geophys. Res.*, *107*, 1384, doi:10.1029/2001JA005088.

Elkington, S. R., M. K. Hudson, and A. A. Chan (2003), Resonant acceleration and diffusion of outer zone electrons in an asymmetric geomagnetic field, *J. Geophys. Res.*, *108*, 1116, doi:10.1029/2001JA009202.

Ellacott, S. W., and W. P. Wilkinson (2007), Heating of directly transmitted ions at low Mach number oblique collisionless shocks: A statistical physics formulation, *Planet. Space Sci.*, *55*, 2251–2256, doi:10.1016/j.pss.2007.05.018.

Glassmeier, K.-H., and C. Heppner (1992), Traveling magnetospheric convection twin vortices - Another case study, global characteristics, and a model, *J. Geophys. Res.*, *97*, 3977–3992, doi:10.1029/91JA02464.

Han, D.-S., H. Hietala, X.-C. Chen, Y. Nishimura, L. R. Lyons, J.-J. Liu, H.-Q. Hu, and H.-G. Yang (2017), Observational properties of dayside throat aurora and implications on the possible generation mechanisms, *J. Geophys. Res.*, *122*, 1853–1870, doi: 10.1002/2016JA023394.

Harvey, C. C. (1998), Spatial Gradients and the Volumetric Tensor, *ISSI Scientific Reports Series*, *1*, 307–322.

Hietala, H., and F. Plaschke (2013), On the generation of magnetosheath high-speed jets by bow shock ripples, *J. Geophys. Res.*, *118*, 7237–7245, doi:10.1002/2013JA019172.

Hietala, H., T. V. Laitinen, K. Andréeová, R. Vainio, A. Vaivads, M. Palmroth, T. I. Pulkkinen, H. E. J. Koskinen, E. A. Lucek, and H. Rème (2009), Supermagnetosonic Jets behind a Collisionless Quasiparallel Shock, *Phys. Rev. Lett.*, *103*(24), 245001, doi: 10.1103/PhysRevLett.103.245001.

Hietala, H., N. Partamies, T. V. Laitinen, L. B. N. Clausen, G. Facskó, A. Vaivads, H. E. J. Koskinen, I. Dandouras, H. Rème, and E. A. Lucek (2012), Supermagnetosonic subsolar magnetosheath jets and their effects: from the solar wind to the ionospheric convection, *Ann. Geophys.*, *30*, 33–48, doi:10.5194/angeo-30-33-2012.

Karimabadi, H., V. Roytershteyn, H. Vu, Y. Omelchenko, J. Scudder, W. Daughton, A. Dimmock, K. Nykyri, M. Wan, D. Sibeck, et al. (2014), The link between shocks, turbulence, and magnetic reconnection in collisionless plasmas, *Physics of Plasmas (1994-present)*, *21*(6), 062,308.

Karlsson, T., N. Brenning, H. Nilsson, J.-G. Trotignon, X. Vallières, and G. Facsko (2012), Localized density enhancements in the magnetosheath: Three-dimensional morphology and possible importance for impulsive penetration, *J. Geophys. Res.*, *117*, A03227, doi: 10.1029/2011JA017059.

King, J. H., and N. E. Papitashvili (2005), Solar wind spatial scales in and comparisons of hourly Wind and ACE plasma and magnetic field data, *J. Geophys. Res.*, *110*, A02104, doi:10.1029/2004JA010649.

Lin, Y. (1997), Generation of anomalous flows near the bow shock by its interaction with interplanetary discontinuities, *J. Geophys. Res.*, *102*, 24,265–24,282, doi: 10.1029/97JA01989.

Lin, Y., L. C. Lee, and M. Yan (1996a), Generation of dynamic pressure pulses downstream of the bow shock by variations in the interplanetary magnetic field orientation, *J. Geophys. Res.*, *101*, 479–493, doi:10.1029/95JA02985.

Lin, Y., D. W. Swift, and L. C. Lee (1996b), Simulation of pressure pulses in the bow shock and magnetosheath driven by variations in interplanetary magnetic field direction,, *J. Geophys. Res.*, *101*, 27,251–27,269, doi:10.1029/96JA02733.

Němeček, Z., J. Šafránková, L. Přech, D. G. Sibeck, S. Kokubun, and T. Mukai (1998), Transient flux enhancements in the magnetosheath, *Geophys. Res. Lett.*, *25*, 1273–1276, doi:10.1029/98GL50873.

Němeček, Z., J. Šafránková, L. Přech, G. N. Zastenker, K. I. Paularena, and S. Kokubun (2000), Magnetosheath Study: Interball Observation, *Adv. Space Res.*, *25*, 1511–1516, doi:10.1016/S0273-1177(99)00663-8.

Němeček, Z., J. Šafránková, G. N. Zastenker, P. Pišoft, and K. Jelínek (2002), Low-frequency variations of the ion flux in the magnetosheath, *Planet. Space Sci.*, *50*, 567–575, doi:10.1016/S0032-0633(02)00036-3.

Omidi, N., and D. G. Sibeck (2007), Formation of hot flow anomalies and solitary shocks, *J. Geophys. Res.*, *112*, A01203, doi:10.1029/2006JA011663.

Omidi, N., X. Blanco-Cano, and C. T. Russell (2005), Macrostructure of collisionless bow shocks: 1. Scale lengths, *J. Geophys. Res.*, *110*(A9), A12212, doi: 10.1029/2005JA011169.

Plaschke, F., and K.-H. Glassmeier (2011), Properties of standing Kruskal-Schwarzschild-modes at the magnetopause, *Ann. Geophys.*, *29*, 1793–1807, doi:10.5194/angeo-29-1793-2011.

Plaschke, F., K.-H. Glassmeier, H. U. Auster, O. D. Constantinescu, W. Magnes, V. Angelopoulos, D. G. Sibeck, and J. P. McFadden (2009), Standing Alfvén waves at the magnetopause, *Geophys. Res. Lett.*, *36*, L02104, doi:10.1029/2008GL036411.

Plaschke, F., H. Hietala, and V. Angelopoulos (2013), Anti-sunward high-speed jets in the subsolar magnetosheath, *Ann. Geophys.*, *31*, 1877–1889, doi:10.5194/angeo-31-1877-2013.

Plaschke, F., H. Hietala, V. Angelopoulos, and R. Nakamura (2016a), Geoeffective jets impacting the magnetopause are very common, *J. Geophys. Res.*, *121*, 3240–3253, doi: 10.1002/2016JA022534.

Plaschke, F., N. Kahr, D. Fischer, R. Nakamura, W. Baumjohann, W. Magnes, J. L. Burch, R. B. Torbert, C. T. Russell, B. L. Giles, R. J. Strangeway, H. K. Leinweber, K. R. Bromund, B. J. Anderson, G. Le, M. Chutter, J. A. Slavin, and E. L. Kepko (2016b), Steepening of waves at the duskside magnetopause, *Geophys. Res. Lett.*, *43*, 7373–7380, doi: 10.1002/2016GL070003.

Pollock, C., T. Moore, A. Jacques, J. Burch, U. Gliese, Y. Saito, T. Omoto, L. Avanov, A. Barrie, V. Coffey, J. Dorelli, D. Gershman, B. Giles, T. Rosnack, C. Salo, S. Yokota, M. Adrian, C. Aoustin, C. Auletti, S. Aung, V. Bigio, N. Cao, M. Chandler, D. Chornay, K. Christian, G. Clark, G. Collinson, T. Corris, A. DeăLosăSantos, R. Devlin, T. Diaz, T. Dickerson, C. Dickson, A. Diekmann, F. Diggs, C. Duncan, A. Figueroa-

Vinas, C. Firman, M. Freeman, N. Galassi, K. Garcia, G. Goodhart, D. Guererro, J. Hageman, J. Hanley, E. Hemminger, M. Holland, M. Hutchins, T. James, W. Jones, S. Kreisler, J. Kujawski, V. Lavu, J. Lobell, E. LeCompte, A. Lukemire, E. MacDonald, A. Mariano, T. Mukai, K. Narayanan, Q. Nguyan, M. Onizuka, W. Paterson, S. Persyn, B. Piepgrass, F. Cheney, A. Rager, T. Raghuram, A. Ramil, L. Reichenthal, H. Rodriguez, J. Rouzaud, A. Rucker, M. Samara, J.-A. Sauvaud, D. Schuster, M. Shappirio, K. Shelton, D. Sher, D. Smith, K. Smith, S. Smith, D. Steinfeld, R. Szymkiewicz, K. Tanimoto, J. Taylor, C. Tucker, K. Tull, A. Uhl, J. Vloet, P. Walpole, S. Weidner, D. White, G. Winkert, P.-S. Yeh, and M. Zeuch (2016), Fast plasma investigation for magnetospheric multiscale, *Space Sci. Rev.*, *199*(1), 331–406, doi:10.1007/s11214-016-0245-4.

Robert, P., A. Roux, C. C. Harvey, M. W. Dunlop, P. W. Daly, and K.-H. Glassmeier (1998), Tetrahedron Geometric Factors, *ISSI Scientific Reports Series*, *1*, 323–348.

Russell, C. T., B. J. Anderson, W. Baumjohann, K. R. Bromund, D. Dearborn, D. Fischer, G. Le, H. K. Leinweber, D. Leneman, W. Magnes, J. D. Means, M. B. Moldwin, R. Nakamura, D. Pierce, F. Plaschke, K. M. Rowe, J. A. Slavin, R. J. Strangeway, R. Torbert, C. Hagen, I. Jernej, A. Valavanoglou, and I. Richter (2016), The Magnetospheric Multiscale Magnetometers, *Space Sci. Rev.*, *199*(1), 189–256, doi:10.1007/s11214-014-0057-3.

Savin, S., E. Amata, L. Zelenyi, V. Budaev, G. Consolini, R. Treumann, E. Lucek, J. Safrankova, Z. Nemecek, Y. Khotyaintsev, M. Andre, J. Buechner, H. Alleyne, P. Song, J. Blecki, J. L. Rauch, S. Romanov, S. Klimov, and A. Skalsky (2008), High energy jets in the Earth's magnetosheath: Implications for plasma dynamics and anomalous transport, *J. Exp. Theor. Phys. Lett.*, *87*, 593–599, doi:10.1134/S0021364008110015.

Savin, S., V. Budaev, L. Zelenyi, E. Amata, D. Sibeck, V. Lutsenko, N. Borodkova, H. Zhang, V. Angelopoulos, J. Safrankova, Z. Nemecek, J. Blecki, J. Buechner, L. Kozak, S. Romanov, A. Skalsky, and V. Krasnoselsky (2011), Anomalous interaction of a plasma flow with the boundary layers of a geomagnetic trap, *J. Exp. Theor. Phys. Lett.*, *93*, 754–762, doi:10.1134/S0021364011120137.

Savin, S., E. Amata, L. Zelenyi, Z. Nemecek, N. Borodkova, J. Buechner, D. P. W., E. A. Kronberg, J. Blecki, J. Budaev, L. Kozak, S. A., and L. Lezhen (2012), Super fast plasma streams as drivers of transient and anomalous magnetospheric dynamics, *Ann. Geophys.*, *30*, 1–7, doi:doi:10.5194/angeo-30-1-2012.

Schwartz, S. J., and D. Burgess (1991), Quasi-parallel shocks - A patchwork of three-dimensional structures, *Geophys. Res. Lett.*, *18*, 373–376, doi:10.1029/91GL00138.

Shue, J.-H., J.-K. Chao, P. Song, J. P. McFadden, A. Suvorova, V. Angelopoulos, K. H. Glassmeier, and F. Plaschke (2009), Anomalous magnetosheath flows and distorted subsolar magnetopause for radial interplanetary magnetic fields, *Geophys. Res. Lett.*, *36*, L18112, doi:10.1029/2009GL039842.

Sibeck, D. G., and J. T. Gosling (1996), Magnetosheath density fluctuations and magnetopause motion, *J. Geophys. Res.*, *101*, 31–40, doi:10.1029/95JA03141.

Sibeck, D. G., K. Kudela, R. P. Lepping, R. Lin, Z. Nemecek, M. N. Nozdrachev, T.-D. Phan, L. Prech, J. Safrankova, H. Singer, and Y. Yermolaev (2000), Magnetopause motion driven by interplanetary magnetic field variations, *J. Geophys. Res.*, *105*, 25,155–25,170, doi:10.1029/2000JA900109.

Torbert, R. B., C. T. Russell, W. Magnes, R. E. Ergun, P.-A. Lindqvist, O. LeContel, H. Vaith, J. Macri, S. Myers, D. Rau, J. Needell, B. King, M. Granoff, M. Chutter, I. Dors, G. Olsson, Y. V. Khotyaintsev, A. Eriksson, C. A. Kletzing, S. Bounds, B. Anderson, W. Baumjohann, M. Steller, K. Bromund, G. Le, R. Nakamura, R. J. Strangeway, H. K. Leinweber, S. Tucker, J. Westfall, D. Fischer, F. Plaschke, J. Porter, and K. Lappalainen (2016), The FIELDS Instrument Suite on MMS: Scientific Objectives, Measurements, and Data Products, *Space Sci. Rev.*, *199*(1), 105–135, doi:10.1007/s11214-014-0109-8.

Turner, D. L., Y. Shprits, M. Hartinger, and V. Angelopoulos (2012), Explaining sudden losses of outer radiation belt electrons during geomagnetic storms, *Nat. Phys.*, *8*, 208–212, doi:10.1038/nphys2185.

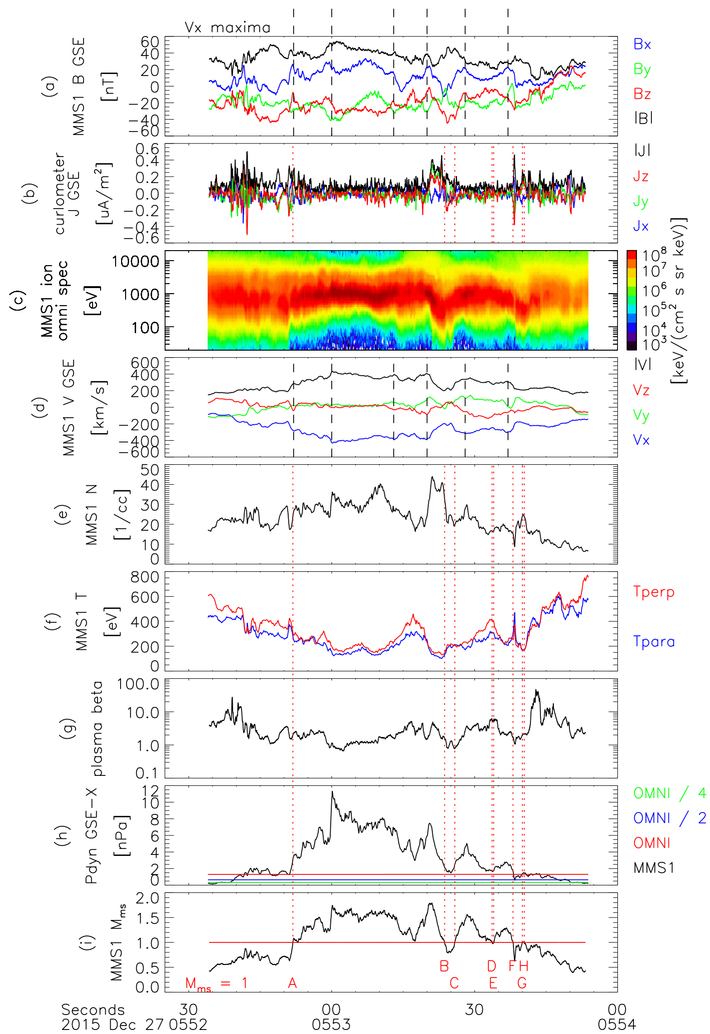

Figure 4. Close-up of leading jet. MMS burst mode measurements on 27 December 2015 between 05:52:25 and 05:54:00 UT. From top to bottom: (a) MMS1 FGM $\vec{B}$ in GSE, (b) curlometer current density $\vec{J}$ in GSE, (c) MMS1 FPI ion omni-directional differential energy flux, (d) MMS1 FPI $\vec{V}$, (e) N, (f) $T_{\parallel}$ and $T_{\perp}$ in blue and red, (g) plasma beta, (h) MMS1 $P_{\mathrm{dyn},x}$ in black and OMNI solar wind dynamic pressures in red (half and one quarter thereof in blue and green), and (i) local magnetosonic Mach number M_{ms} at MMS1 in the spacecraft's frame of reference. The vertical black dashed lines indicate local maxima in V_x. The vertical red dotted lines mark instances where $M_{\mathrm{ms}} = 1$; they are numbered in panel (i) with letters A to H.

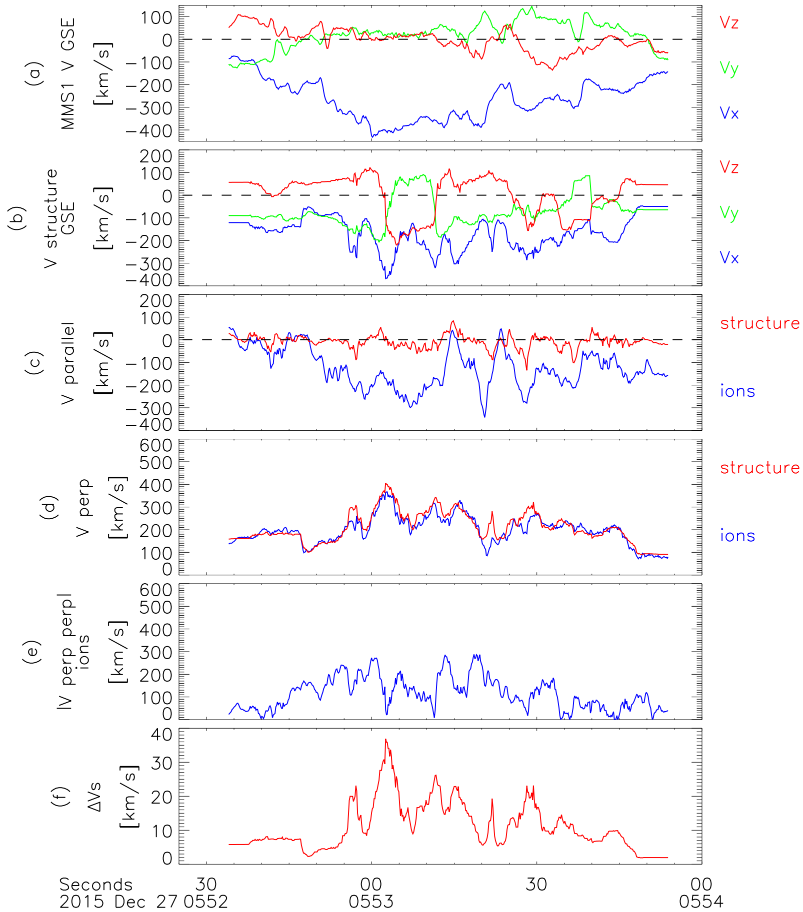

Figure 5. Velocity of structures/waves $\vec{V}_s$ manifesting themselves as magnetic field fluctuations and comparison with the ion velocity $\vec{V}$. From top to bottom: (a) MMS1 FPI ion velocity $\vec{V}$, (b) structure velocity $\vec{V}_s$, (c) ion $\vec{V}$ (blue) and $\vec{V}_s$ (red) parallel to $\vec{B}$ ($V_{\|}$ and $V_{s\|}$), (d) $\vec{V}_s$ component perpendicular to $\vec{B}$ ($|\vec{V}_{s\perp}|$, red) and ion $\vec{V}$ component parallel to $\vec{V}_{s\perp}$ ($V_{\perp}$, blue), (e) absolute value of the ion velocity component perpendicular to $\vec{B}$ and to $\vec{V}_{s\perp}$: $V_{\perp\perp}$, and (f) uncertainty ΔV_s of $\vec{V}_s$. Note that panels (a) to (e) have the same scale.

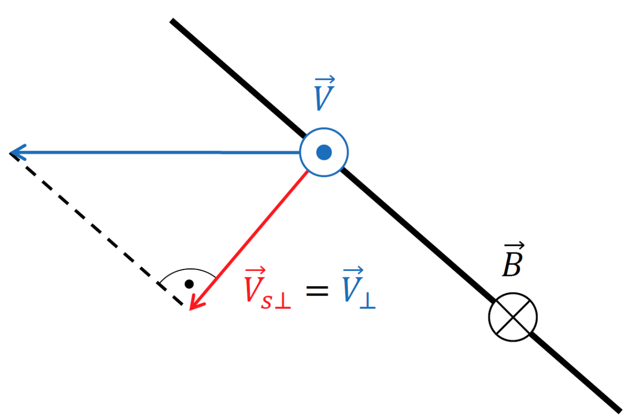

Figure 6. A structure/current sheet (black solid line) with normal direction locally perpendicular to $\vec{B}$ that moves with the plasma at velocity $\vec{V}$ will propagate with velocity $V_{s\perp} = V_{\perp}$ along that normal direction. By that motion, plasmas do not cross the structure/sheet.

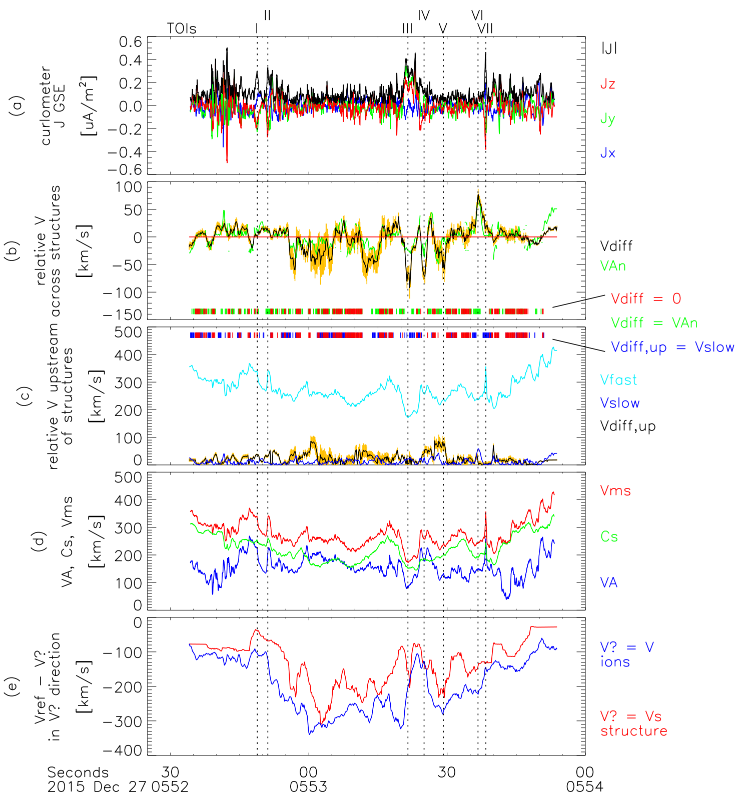

Figure 7. Comparison of the velocities of magnetic field structures or wave fronts with characteristic speeds of the plasma. From top to bottom: (a) Curlometer current density $\vec{J}$ in GSE, (b) V_{diff} in black and structure normal Alfvén velocity $\pm V_{\text{A}n}$ adjusted to the sign of V_{diff} in green, (c) $|V_{\text{diff,up}}|$ determined with time-shifted ion velocity data upstream of structures in black, V_{slow} in dark blue and V_{fast} in light blue, (d) Alfvén, sound, and magnetosonic velocities (V_{A}, C_{s}, and V_{ms} in blue, green, and red), and (e) $(\vec{V}_{\text{ref}} - \vec{V}_{\text{s}}) \cdot (\vec{V}_{\text{s}}/|\vec{V}_{\text{s}}|)$ in red and $(\vec{V}_{\text{ref}} - \vec{V}) \cdot (\vec{V}/|\vec{V}|)$ in blue. The yellow areas in panels (b) and (c) mark the uncertainty level ΔV_{s} of V_{diff} and $V_{\text{diff,up}}$. The vertical black dotted lines mark times of interest, corresponding with current density enhancements or V_{diff} peaks. They are numbered with roman numerals at the top of the figure. Colored bars in panels (b) and (c): red shows $V_{\text{diff}} \approx 0\,\text{km/s}$, green indicates $V_{\text{diff}} \approx V_{\text{A}n}$, and blue shows $V_{\text{diff,up}} \approx V_{\text{slow}}$ (within uncertainty levels).

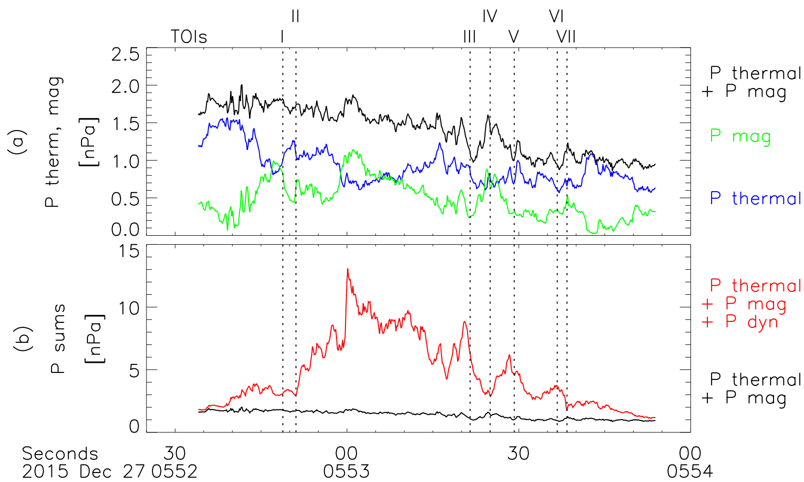

Figure 8. Pressures associated with jet number 1: (a) MMS1 thermal pressure $P_{\text{thermal}} = NT_{\perp}$ (blue), magnetic pressure $P_{\text{mag}} = B^2/(2\mu_0)$ (green), and the sum of the two pressures in black, and (b) sum of $P_{\text{thermal}} + P_{\text{mag}}$ (black) and $P_{\text{thermal}} + P_{\text{mag}} + P_{\text{dyn},x}$ (red). The vertical black dotted lines depict TOIs (same as Figure 7).

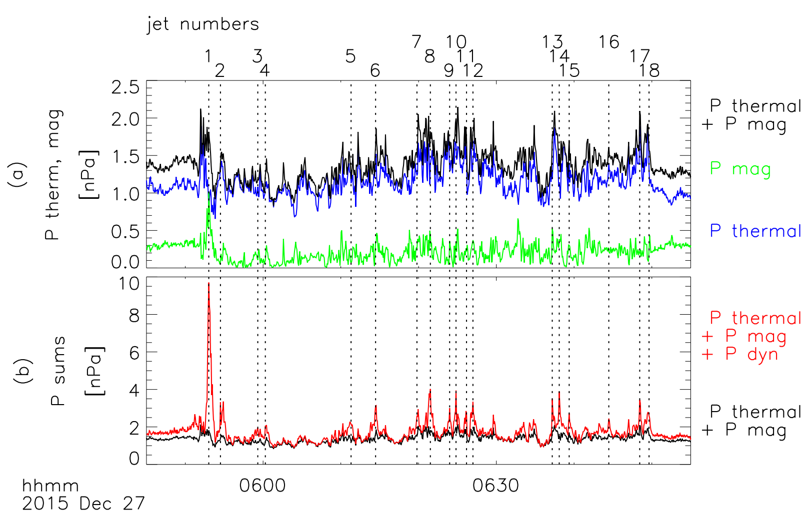

Figure 9. Pressures in the interval of interest, derived from MMS1 fast survey data: (a) MMS1 thermal pressure $P_{\text{thermal}} = NT_{\perp}$ (blue), magnetic pressure $P_{\text{mag}} = B^2/(2\mu_0)$ (green), and the sum of the two pressures in black, and (b) sum of $P_{\text{thermal}} + P_{\text{mag}}$ (black) and $P_{\text{thermal}} + P_{\text{mag}} + P_{\text{dyn},x}$ (red). The vertical black dotted lines depict jet observation times.

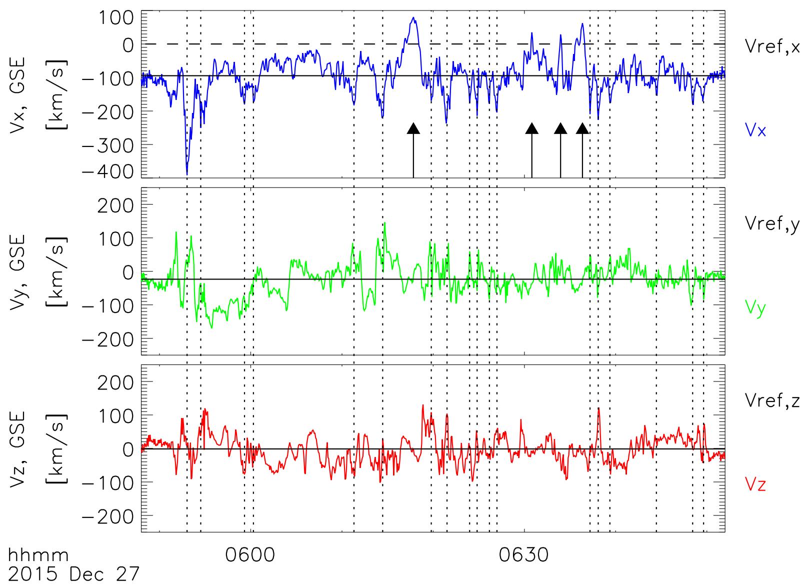

Figure 10. Ion velocity measurements in GSE by MMS1 on 27 December 2015 between 05:48 and 06:52 UT. Reference velocity $\vec{V}_{\text{ref}}$ shown in black. Dotted vertical lines mark jets 1 to 18. The arrows mark sunward magnetosheath plasma flows ($V_x > 0$ in GSE, where $V_x = 0$ is depicted by a horizontal dashed line).

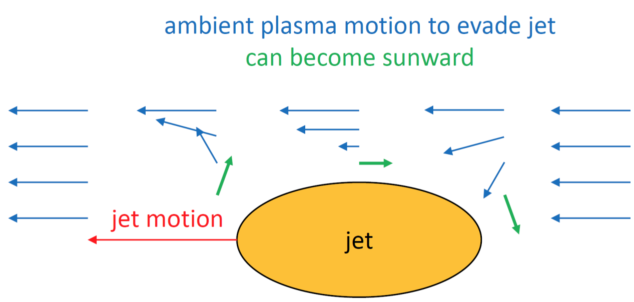

Figure 11. Illustration showing the motion of magnetosheath plasma in the vicinity of a jet.

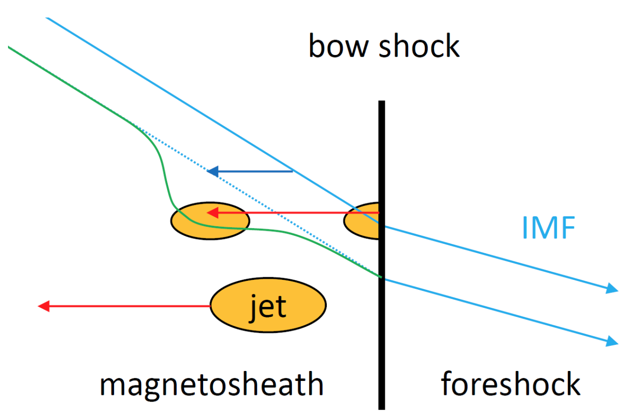

Figure 12. Illustration of how the plasma motion of a high-speed jet (red arrow) through slower ambient plasma (blue arrow) modifies the magnetic field in the magnetosheath (green line).

Figure 1.

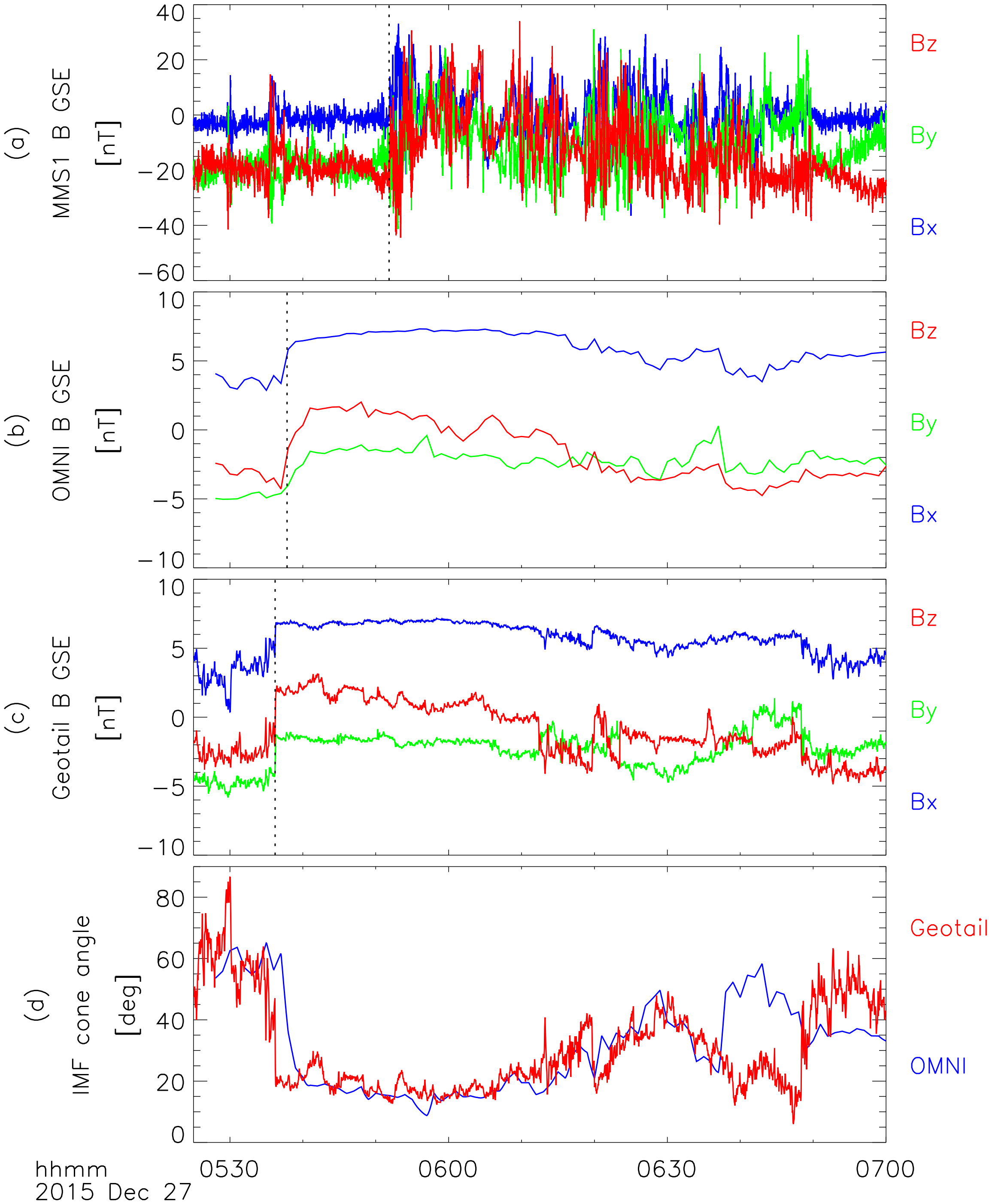
(a)
MMS1 B GSE
[nT]
40
20
0
−20
−40
−60
Bz
By
Bx
(b)
OMNI B GSE
[nT]
10
5
0
−5
−10
Bz
By
Bx
(c)
Geotail B GSE
[nT]
10
5
0
−5
−10
Bz
By
Bx
(d)
IMF cone angle
[deg]
80
60
40
20
0
Geotail
OMNI
hhmm
2015 Dec 27
0530
0600
0630
0700

Figure 2.

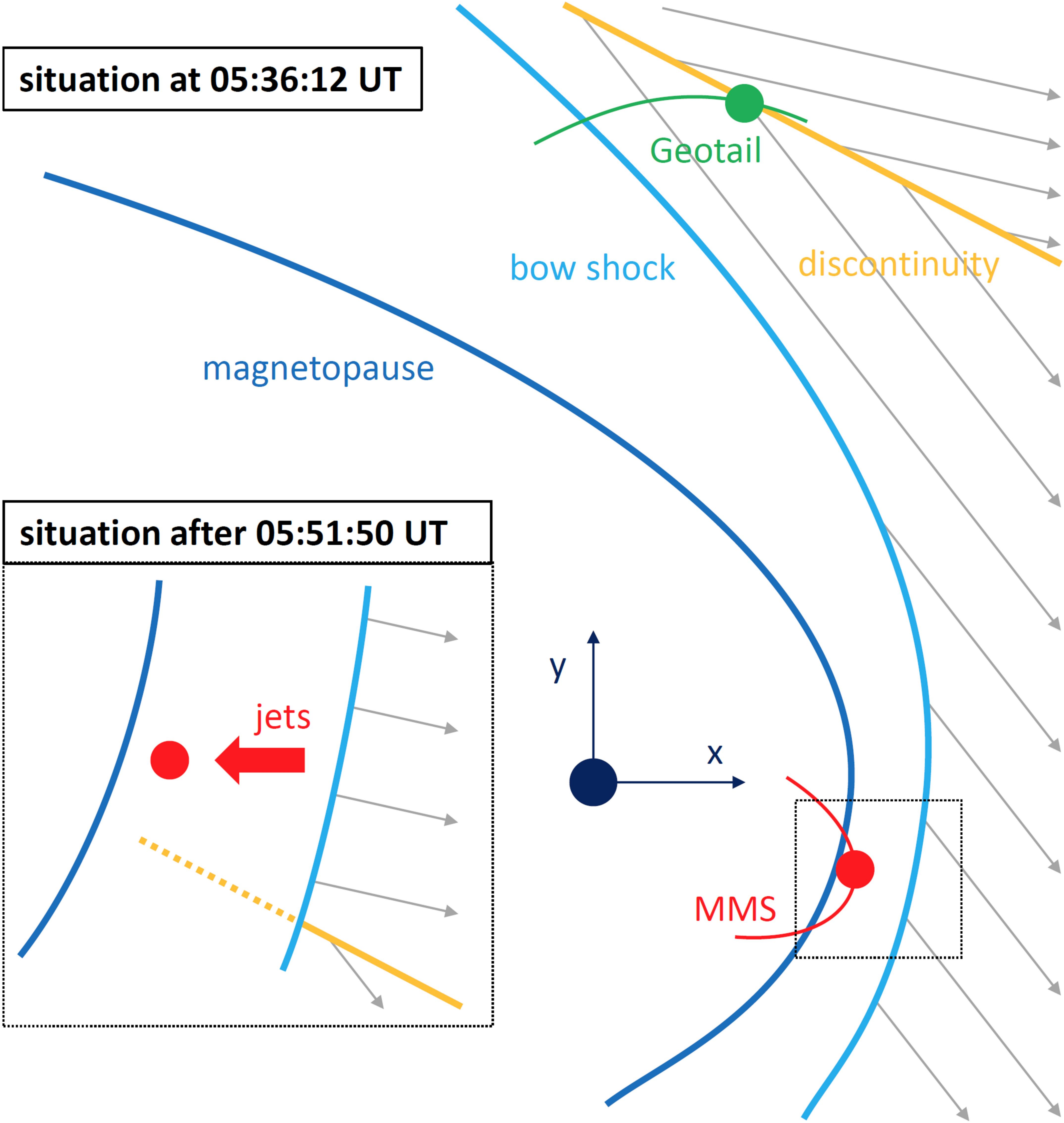
situation at 05:36:12 UT
Geotail
bow shock
discontinuity
magnetopause
situation after 05:51:50 UT
jets
y
x
MMS

Figure 3.

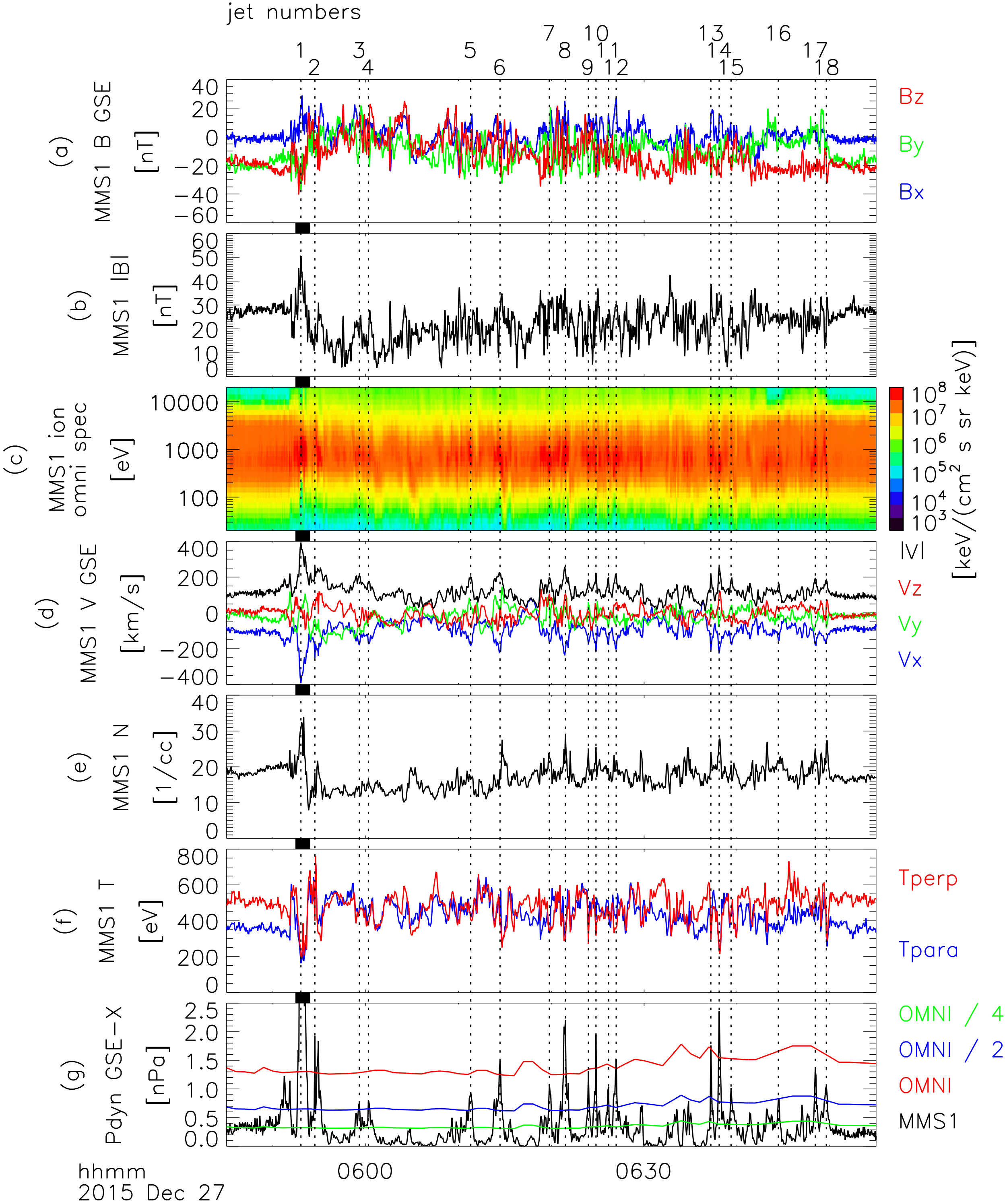

jet numbers
1 2 3 4 5 6 7 8 9 10 11 12 13 14 15 16 17 18
(a) MMS1 B GSE [nT]
40 20 0 −20 −40 −60
Bz
By
Bx
(b) MMS1 |B| [nT]
60 50 40 30 20 10 0
(c) MMS1 ion omni spec [eV]
10000 1000 100
10^8 10^7 10^6 10^5 10^4 10^3
[keV/(cm^2 s sr keV)]
(d) MMS1 V GSE [km/s]
400 200 0 −200 −400
|V|
Vz
Vy
Vx
(e) MMS1 N [1/cc]
40 30 20 10 0
(f) MMS1 T [eV]
800 600 400 200 0
Tperp
Tpara
(g) Pdyn GSE−X [nPa]
2.5 2.0 1.5 1.0 0.5 0.0
OMNI / 4
OMNI / 2
OMNI
MMS1
hhmm
2015 Dec 27
0600
0630

Figure 4.

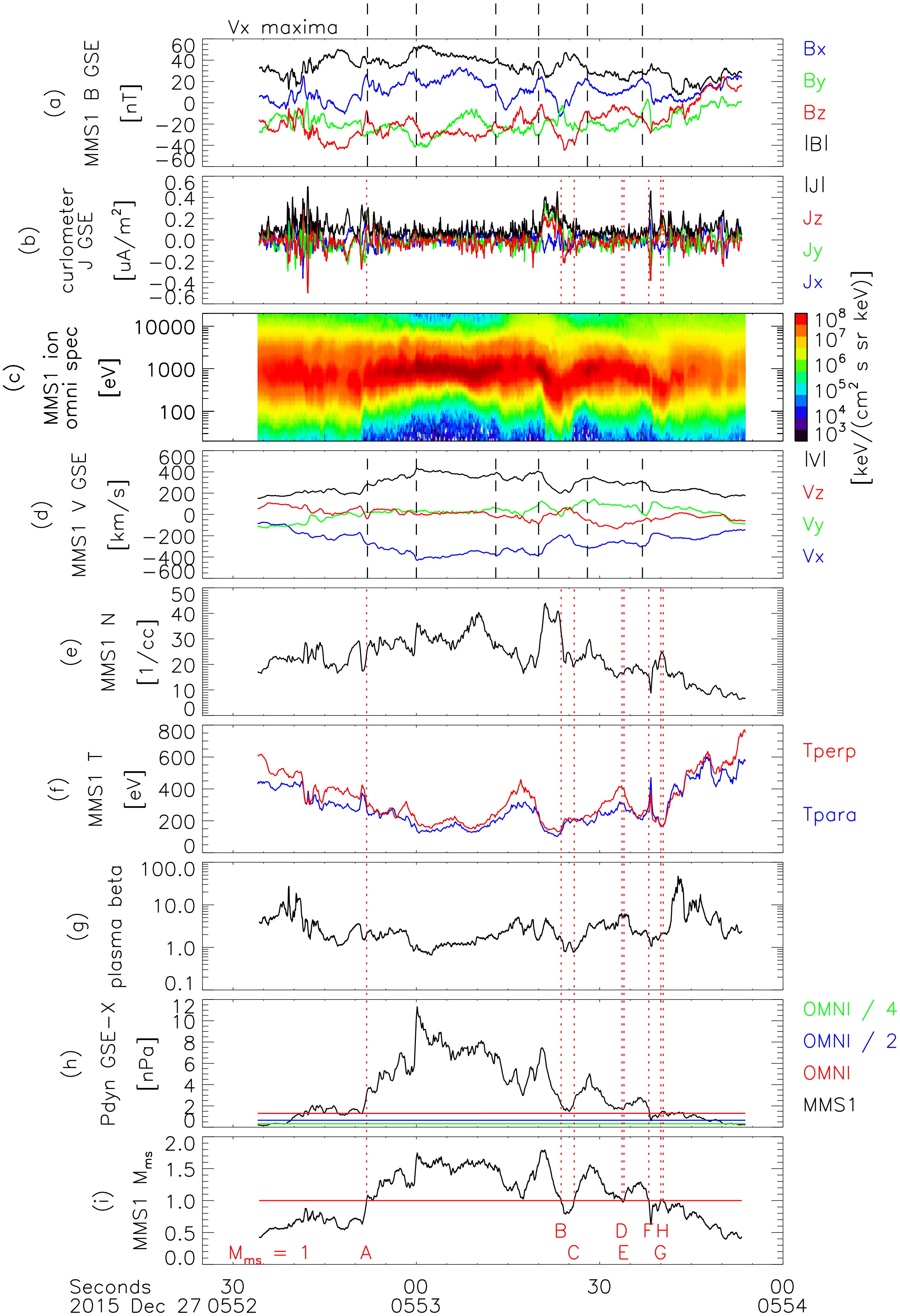
Vx maxima
(a) MMS1 B GSE [nT]
Bx
By
Bz
|B|
(b) curlometer J GSE [uA/m^2]
|J|
Jz
Jy
Jx
(c) MMS1 ion omni spec [eV]
[keV/(cm^2 s sr keV)]
(d) MMS1 V GSE [km/s]
|V|
Vz
Vy
Vx
(e) MMS1 N [1/cc]
(f) MMS1 T [eV]
Tperp
Tpara
(g) plasma beta
(h) Pdyn GSE−X [nPa]
OMNI / 4
OMNI / 2
OMNI
MMS1
(i) MMS1 M_ms
M_ms = 1
A
B
C
D
E
F
G
H
Seconds
2015 Dec 27 0552
0553
0554

Figure 5.

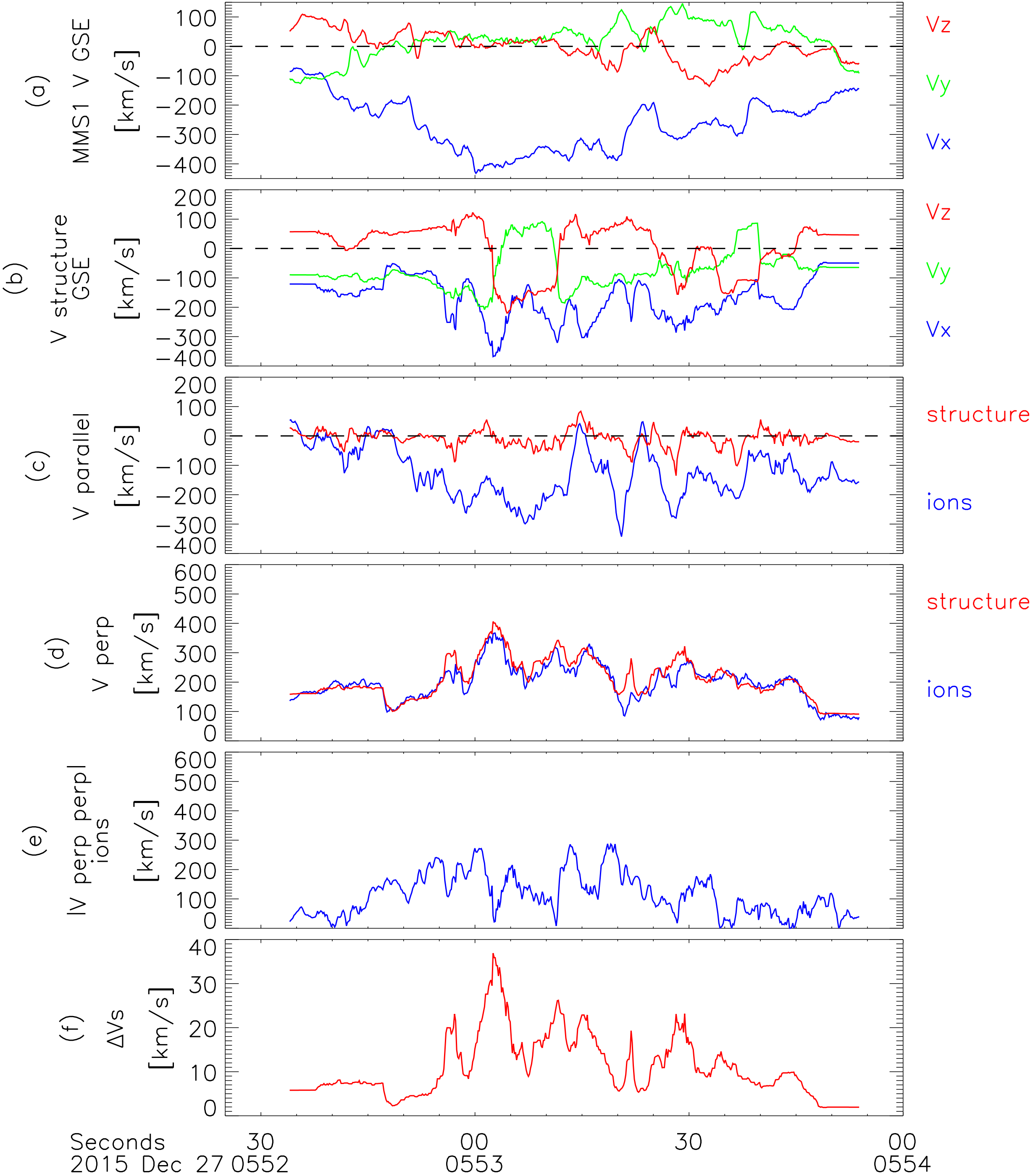

(a)
MMS1 V GSE
[km/s]
100
0
−100
−200
−300
−400
Vz
Vy
Vx
(b)
V structure
GSE
[km/s]
200
100
0
−100
−200
−300
−400
Vz
Vy
Vx
(c)
V parallel
[km/s]
200
100
0
−100
−200
−300
−400
structure
ions
(d)
V perp
[km/s]
600
500
400
300
200
100
0
structure
ions
(e)
|V perp perp|
ions
[km/s]
600
500
400
300
200
100
0
(f)
ΔVs
[km/s]
40
30
20
10
0
Seconds
2015 Dec 27 0552
30
00
0553
30
00
0554

Figure 6.

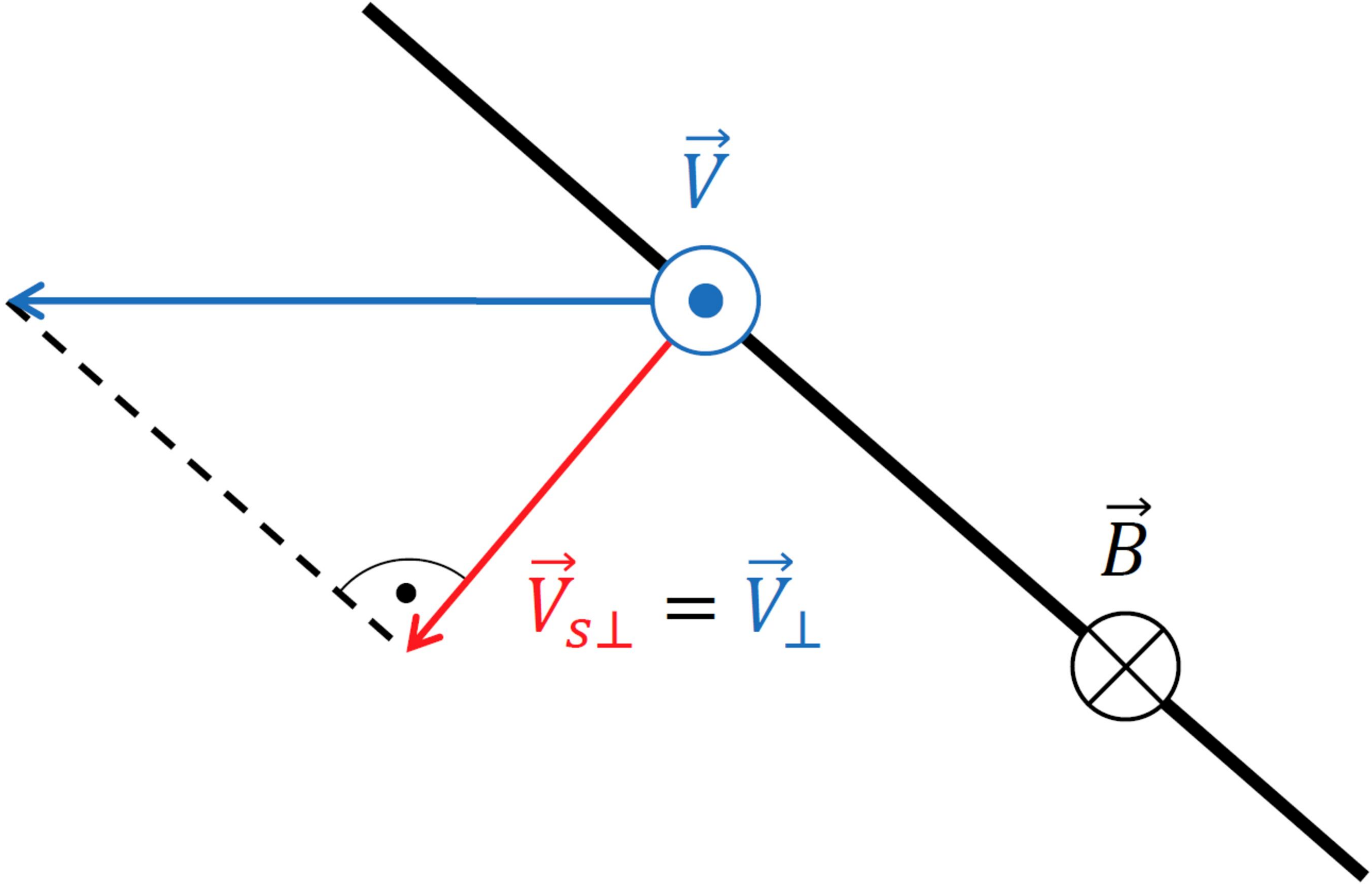
$\vec{V}$
$\vec{B}$
$\vec{V}_{s\perp} = \vec{V}_{\perp}$

Figure 7.

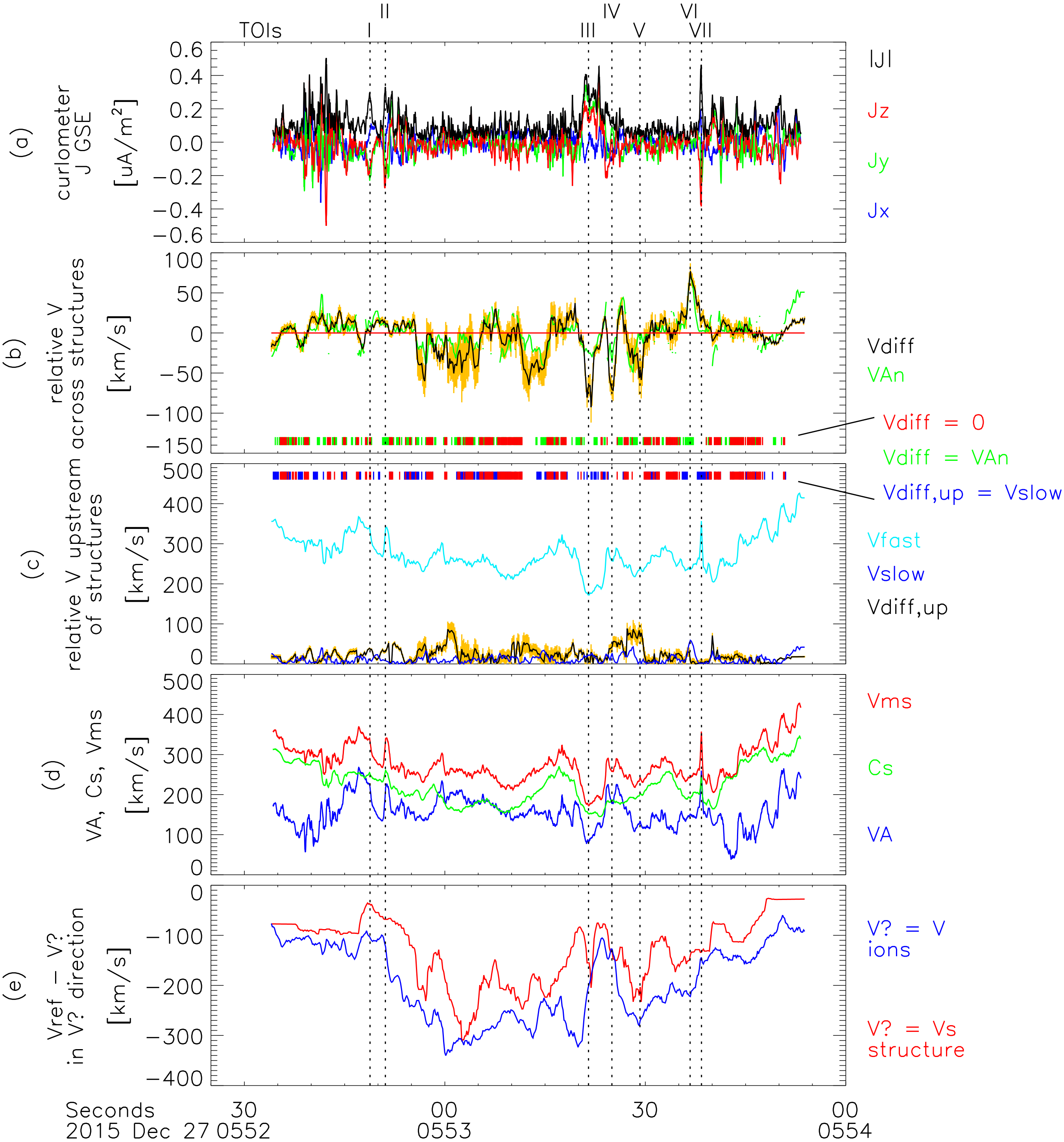

TOIs
I
II
III
IV
V
VI
VII
(a) curlometer J GSE [uA/m^2]
|J|
Jz
Jy
Jx
(b) relative V across structures [km/s]
Vdiff
VAn
Vdiff = 0
Vdiff = VAn
(c) relative V upstream of structures [km/s]
Vdiff,up = Vslow
Vfast
Vslow
Vdiff,up
(d) VA, Cs, Vms [km/s]
Vms
Cs
VA
(e) Vref − V? in V? direction [km/s]
V? = V ions
V? = Vs structure
Seconds
2015 Dec 27 0552
30
00
0553
30
00
0554

Figure 8.

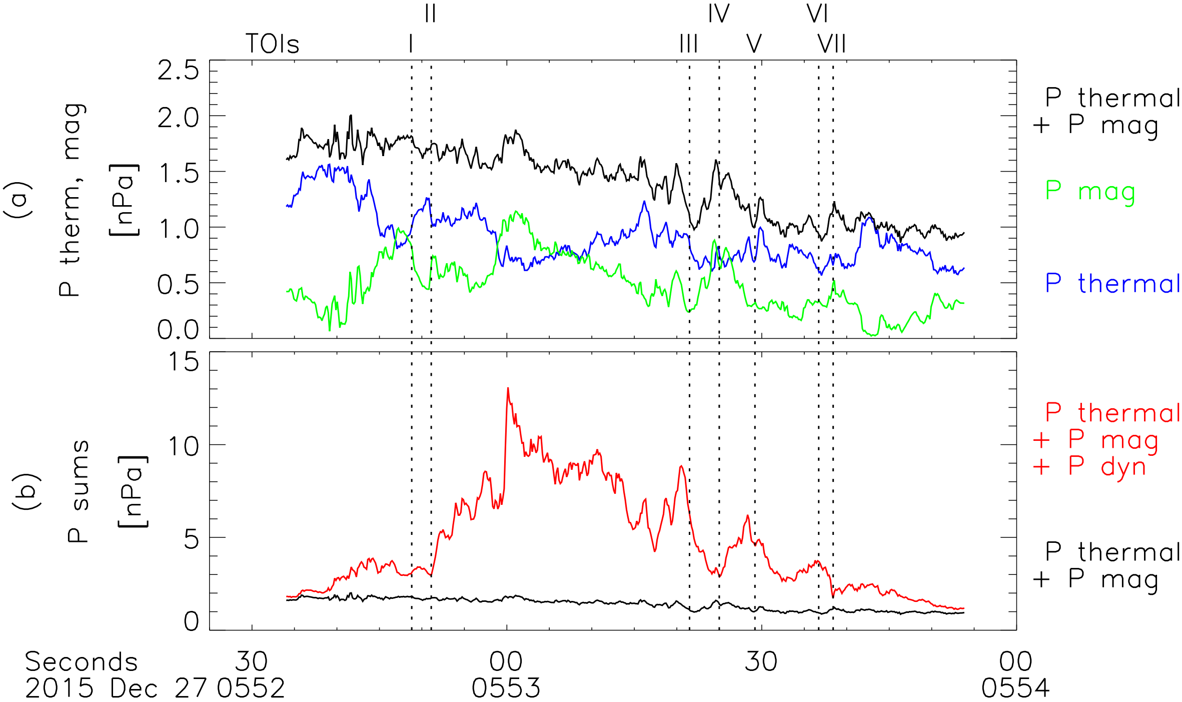

TOIs
I
II
III
IV
V
VI
VII
(a)
P therm, mag
[nPa]
2.5
2.0
1.5
1.0
0.5
0.0
P thermal
+ P mag
P mag
P thermal
(b)
P sums
[nPa]
15
10
5
0
P thermal
+ P mag
+ P dyn
P thermal
+ P mag
Seconds
2015 Dec 27 0552
30
00
0553
30
00
0554

Figure 9.

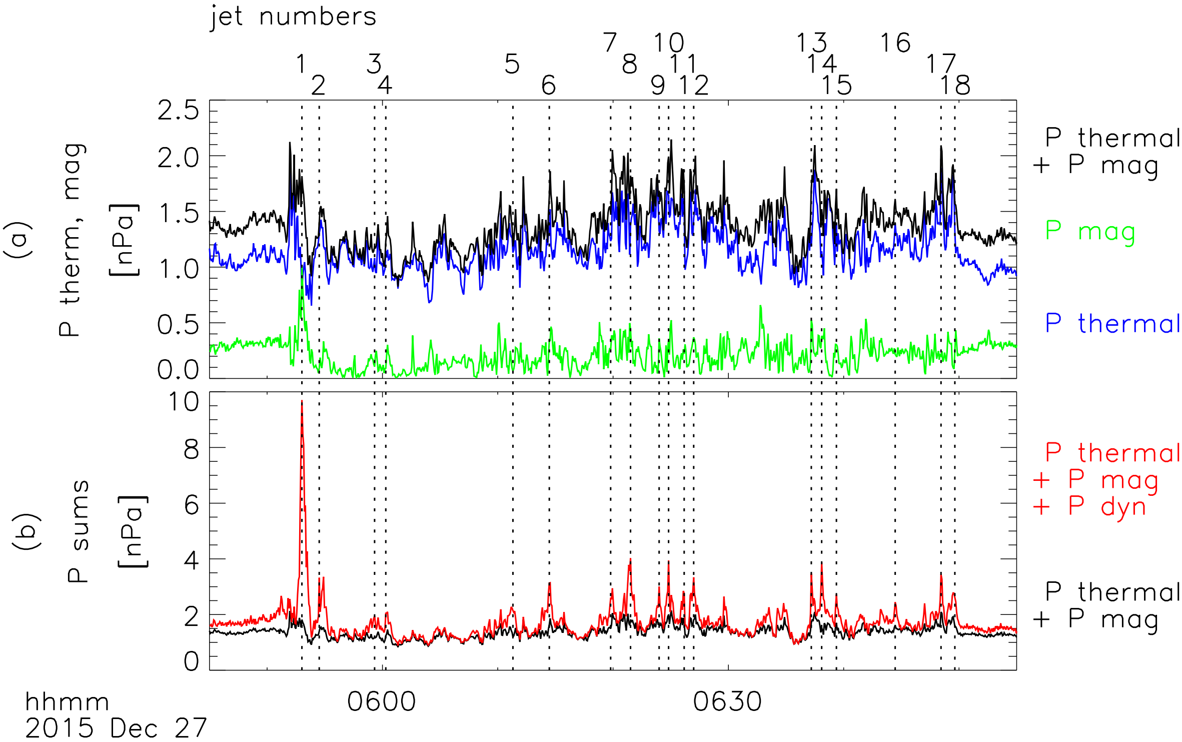
jet numbers
1 2 3 4 5 6 7 8 9 10 11 12 13 14 15 16 17 18
(a) P therm, mag [nPa]
2.5
2.0
1.5
1.0
0.5
0.0
P thermal + P mag
P mag
P thermal
(b) P sums [nPa]
10
8
6
4
2
0
P thermal + P mag + P dyn
P thermal + P mag
hhmm
2015 Dec 27
0600
0630

Figure 10.

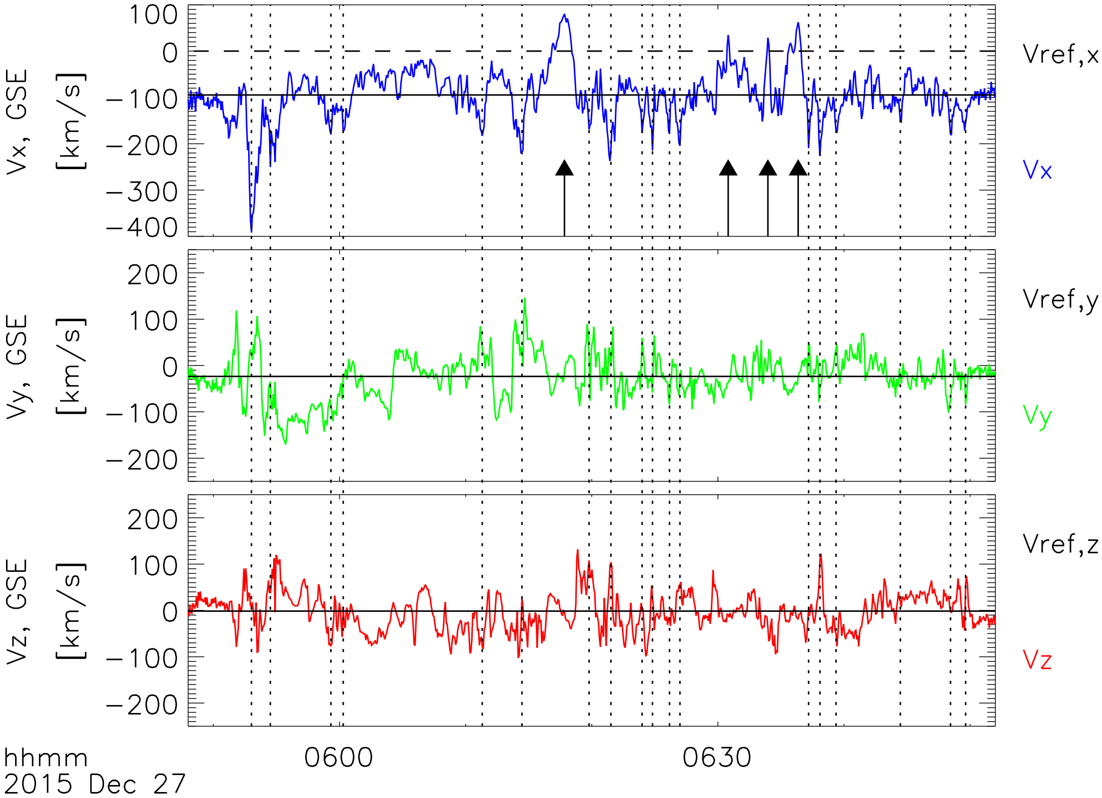

Vx, GSE [km/s]
Vref,x
Vx
Vy, GSE [km/s]
Vref,y
Vy
Vz, GSE [km/s]
Vref,z
Vz
100
0
−100
−200
−300
−400
200
hhmm
2015 Dec 27
0600
0630

Figure 11.

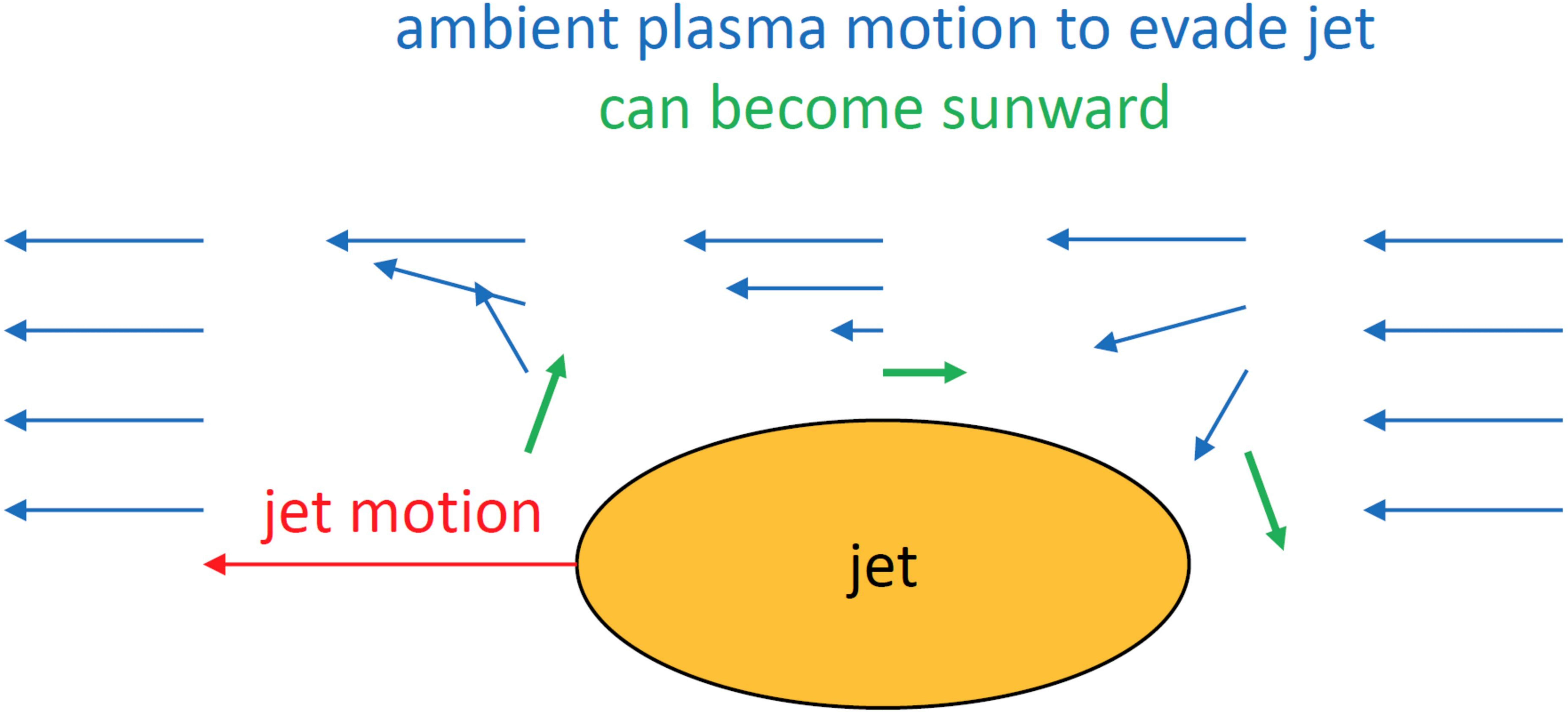
ambient plasma motion to evade jet
can become sunward
jet motion
jet

Figure 12.

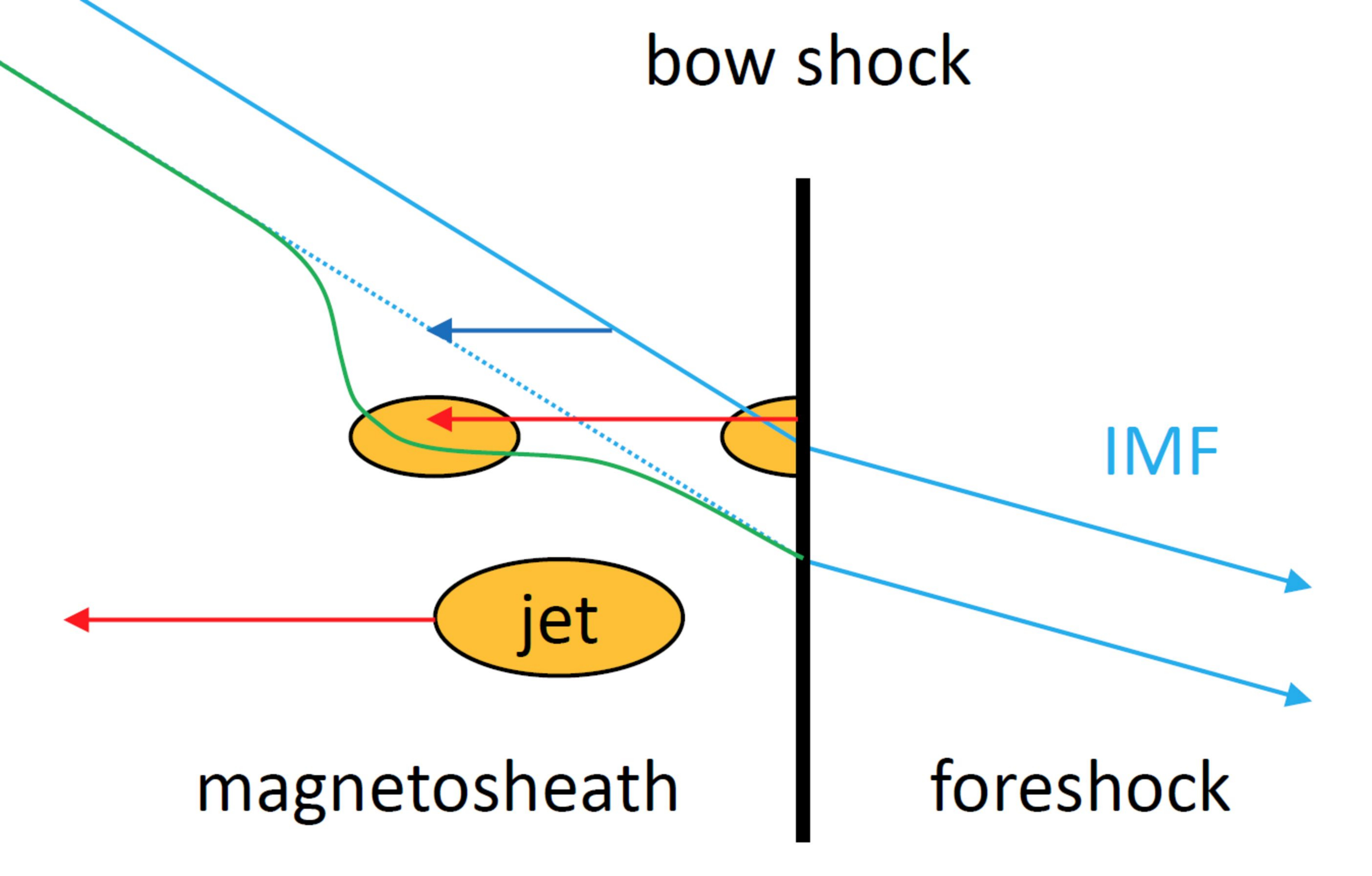
bow shock
IMF
jet
magnetosheath
foreshock